QI TANG
3D ALIGNMENT OF PROJECTIONS IN ELECTRON TO-MOGRAPHY

Master of Science thesis

ABSTRACT

QI TANG: 3D Alignment of Projections in Electron Tomography
Tampere University of Technology
Master of Science thesis, 42 pages
10/16, 2015
Master's Degree Programme in the Faculty of Computing and Electrical Engineering
Major: Signal Processing
Examiner: Prof. Ulla Ruotsalainen, MSc. Erman Acar

Keywords: eletron tomography, alignment, missing wedge, FIRM, conjugate gradient.

The goal of this thesis is to analyze the effect of projection angle errors on reconstructing 3D electron tomography. Noise, missing wedge and miss alignment are three main problems in electron tomography. This thesis focuses on how miss alignment affects the 3D reconstruction relative to the noise and missing wedge effects.

Fourier-based iterative method (FIRM) is the main reconstruction method in this work. Instead of projecting the volume and back-projecting the tilt series in the image domain, FIRM conducts those operations in Frequency domain. By using non-uniform fast Fourier transform, FIRM avoids interpolation problem. Besides, the conjugate gradient method is used as the iterative reconstruction process to find the optimal solution.

With the simulations, the impacts of noise, missing wedge and miss alignment are studied quantitatively. Missing wedge is the most influential factor among those three factors, the lack of enough information causes the reconstruction volume to be highly burred. Miss alignment has a similar effect as Gaussian noise. However, miss alignment also introduces artifacts in the reconstruction. Normalized mean-square error (NMSE) decreases and resolution increases when decreasing the level of miss alignment. After the level of 0.2-degree variance of projection angle error, the results does not show significant differences.

PREFACE

TABLE OF CONTENTS

LIST OF FIGURES

LIST OF ABBREVIATIONS

ART	Algebraic Reconstruction Technique
CG	Conjugate Gradient
DART	Discrete Algebraic Reconstruction Technique
DFT	Discrete Fourier Transform
ET	Electron Tomography
FFT	Fast Fourier Transform
FIRM	Fourier-based Iterative Reconstruction Method
FSC	Fourier Shell Correlation
MSE	Mean-Square Error
NMSE	Normalized Mean-Square Error
NUFFT	Non-Uniform Fast Fourier Transform
SBP	Simple Back-Projection
SIRT	Simultaneous Iterative Reconstruction Technique
sMAP-EM	Sequential Maximum A Posterior-Expectation Maximization
SNR	Signal-to-Noise Ratio
TEM	Transmission Electron Microscope
TVM	Total Variation Minimization
VPE	The Variance of Projection Angle Error
WBP	Weighted Back-Projection

LIST OF SYMBOLS

$\mathbf{A}$	Affine matrix
$\mathbf{H}$	Quaternions
$\mathbf{R}^n$	n-dimensional vector in real space
P	Forward-projection operator
P^{-1}	Back-projection operator
R	The Radon transform operator
R_M	The rotation matrix of forward projection
R_M^T	The rotation matrix of back projection
$\mathbf{T}$	Transformation matrix
S	The Fourier slice
U	The projection image
$\mathbf{V}$	The 3D volume
$\boldsymbol{\alpha}$	The search direction of gradient descent
e	The error term
$\mathbf{m}$	The coordinate of fiducial marker
$\mathbf{p}$	The coordinate of fiducial marker in projection image
$\overrightarrow{u}$	Direction vector in three-dimension space
ϕ	The first Euler angle rotated around z-axis
θ	The second Euler angle rotated around y-axis
ψ	The third Euler angle rotated around z-axis

1. INTRODUCTION

In this thesis, we focus on alignment problem in electron tomography (ET) and analyse its effects on image reconstuction. In this chapter, we start with introducing the background of electron tomography. Then we discuss two major issues in practice, reconstruction of the 3D volume from limited number of projection images and the miss-alignment of the projection images during image acquisition. Finally, we give the outline of experiments conducted in this thesis.

1.1   Background

Electron tomography is a technique for obtaining a detailed 3D structure of an object from its series of 2D projection images acquired using a transmission electron microscope (TEM) [1]. In practice, electron tomography contains three different procedures. In the first step, image acquisition, a transmission electron microscope creates a beam of electrons that passes through a volume and collects the information on the 2D plane. The resulting 2D projection images represent the information of this object at different tilt angles. Secondly, the projection images have to be aligned with respect to predefined tilt angles. Since the actual orientation may differ from the predefined angle during image acquisition, the alignment will correct the effect of those unavoidable displacements on reconstruction. At last, the original object is reconstructed from its projection images by using algorithms, such as weighted back projection (WBP) and simultaneous iterative reconstruction technique (SIRT) [2, 3]. Figure 1.1 shows the complete procedure of electron tomography. In practice,
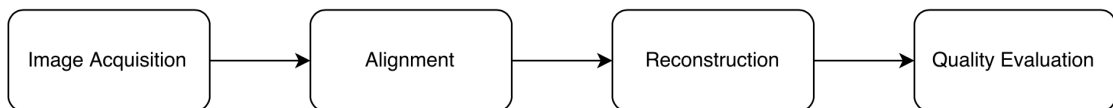

Figure   1.1 *The procedure of electron tomography*

there are several challenges in obtaining high-quality reconstructions [4, 5]. To get a high-resolution observation of object and to understand the highly complex details in the object, researchers have to solve those challenges that appear in alignment and reconstruction procedure [6]. In the next two sections, we describe the conventional solutions for the difficulties and imperfections in reconstruction and alignment process.

1.2 Reconstruction Problem in Electron Tomography

The first problem in the reconstruction process is the low signal-to-noise ratio (SNR), which is a common difficulty in image processing. The noise is introduced during image acquisition and reflected on projection images. However, the noise in electron tomography cannot be easily removed as traditional denoising methods in image processing. Since the reconstruction process transfers the 2D images into a 3D volume by back projection, the noise may be enlarged in the reconstructed volume. As a consequence, the reconstruction will be badly impacted by noise and its resolution will be low as well. As a solution to this problem, Radermacher introduced the weighted back projection (WBP) algorithm [7]. WBP combines the back projection method with a methodically designed filter so that it can alleviate the effect of noise and the blur of back projection. However, the performance of the WBP algorithm depends on the specific analytical forms of the weighting functions, which needs conscientious designs for different samples [8]. Another problem in reconstruction is the missing wedge. Although the projection images contain the information about the object at different tilt angles, the number of projection images is limited in practice. In other words, there is always an unavoidable gap in the available tilt range, and the reconstruction restores the original object with insufficient information. Since WBP is sensitive to limited tilt range, it fails to reconstruct the object with the acceptable quality [9]. As a consequence, the reconstruction quality will be significantly affected without more powerful algorithm. One way to alleviate this problem is the iterative algorithms, such as simultaneous iterative reconstruction technique (SIRT) and discrete algebraic reconstruction technique (DART) [10, 11]. SIRT reprojects reconstruction and back-projects projection images iteratively and updates the reconstructed volume with their difference at each iteration. SIRT generates reconstruction yielding good visual quality from fewer projections and even from noisy data [12]. Whereas, DART combines SIRT with additional prior knowledge. Based on the result of SIRT at each iteration, DART sets a threshold to segment

the reconstruction and select a certain number of boundary pixels as prior information. Only those boundary pixels are updated in each iteration step until the method converges [12]. In this way, reconstruction becomes less-underdetermined. Moreover, DART yields a reconstruction that contains fewer artifacts in comparison to SIRT [13].

The total variation minimization (TVM) method is based on compressive sensing [14, 15]. Compressive sensing is specialized in finding a solution to a set of ill-posed linear equations that has the sparse representation. In electron tomography, the boundaries represent the interface between different compositions, which is sparse. In this way, TVM uses the edge of the specimen as the prior knowledge, which is sparse in the reconstruction. In this way, TVM reduces the elongation artifacts and noise in the reconstruction, and also improves the sharpness of the edge. However, the regularization parameter for the prior knowledge is essential for the reconstruction quality, and is also a computational burden in this algorithm [12].

Due to the disadvantages of computational cost in SIRT and DART, researchers try to find better algorithms for electron tomography. The Fourier-based Iterative Reconstruction Method (FIRM) is faster than SIRT and DART while maintaining comparable performance [16]. Besides, FIRM incorporates prior knowledge so that the results of FIRM are quite accurate. Unlike previous methods, Sequential maximum a posterior expectation maximization (sMAP- EM) method does not use prior knowledge about the specimen searches for the most likely cross-sectional images given the measured projections from TEM [9]. The sMAP-EM algorithm uses a median filtered image of the previous iteration in a weighted one-step-late algorithm as the prior information to control the noise in the reconstructed volume. As a result, this algorithm reduces the noise in the reconstructed volume and estimates values for the missing wedge during the iterations. Besides, the reconstruction process runs sequentially. At each iteration, the previous result initializes the successive one while the weight of the regularization is gradually decreased sequence by sequence [9].

1.3   Alignment Problem in Electron Tomography

For the reconstruction method we mention in previous section 1.2 we suppose to get the projection images ideally at known tilt angles. However, the imaging geometry may not be known or calibrated accurately in practice [17]. For example, the

transmission electron microscope may not move exactly following the instructions, and the object may not be steady during image acquisition. As a consequence, the imaging geometry is always inaccurate, which may create low quality reconstructions. In electron tomography, estimation of the unknown motion parameters of an imaging device or the object is called alignment problem.

Fiducial markers are pervasive tools for aligning projection images since the 1980s. Until now, fiducial markers have been still useful in electron tomography due to its simplicity and straight-forward implementation [18]. In 2007, Brandt proposed a feature-based method that automatically extracts features from the projection images as markers, and tries to use these features to solve the alignment problem [19]. However, the efficiency of the process depends much more on projection images and the projected volume. If those features are hard to detect or the contrast is low, the method is not comparable to fiducial markers. In addition, feature extraction is a computer vision method that identifies features among many projection images [20]. Another famous alignment method is the correlation-based method, which is also called projection matching [21]. However, realignment of the projection images in the real space does not guarantee the improvement of the volume in the object space [22]. Besides, due to its sequential alignment procedure, the error may propagate into subsequent alignment steps if miss-alignment is not fixed in previous steps.

All above alignment methods have one common aspect that they solve the alignment problem before the reconstruction process. Recently, researchers explore new approaches that try to address the problem of alignment simultaneously with the volume reconstruction [19, 23, 22]. These methods map the projection data into spaces in which the data can be conveniently manipulated [24, 25]. In this way, these methods combine the orientation determination and volume reconstruction as a whole convergence process, which optimizes motion parameters and volume estimation for projection images. With an appropriate searching algorithm, these methods could solve the alignment problem in a refinement method. Ideally, the searching algorithm should fulfill two main requirements, rapid convergence, and low computational cost.

1.4   Outline of Experimental Research

In the rest of this thesis, we focus on the problems mentioned above. In Chapter 2, we review various reconstruction methods used in electron tomography and discuss

the reconstruction method utilized in this thesis. Chapter 3 gives more details about alignment methods in electron tomography. Chapter 4 shows the results of the experiments regarding projection acquisition and reconstruction. Chapter 5 summarizes the experiments, analyzes the results, and explains the problems observed and how the results can be improved in the future.

2. 3D RECONSTRUCTION

Tomography is a classical technique deals with the reconstruction of a three-dimensional (3D) object from its two-dimensional (2D) projections. In real life, the projections are measurements of some physical, chemical or other property of the sample integrated over straight lines through the object by using transmission electron microscope. In this chapter, we give the principle of Radon transfom and Fourier slice theorem, so that we could simulate projection process in computer and get numerical samples for later use. The theory part begins with the 2D case for simplicity, but we further analyse the procedures of projection and back-projection in 3D case in the remaining part. At last, we explain different approaches to solving the reconstruction problem.

2.1 Radon Transform and Projections

Radon transform is the foundation of analytical reconstruction method, it relates to the collections of the integrals of a function over straight line [26]. These collections are called projection images, which is the integral over some function. Because there is an extremely related correlation between the parameters of an object and its projection images, we can simulate it using Radon transform. For simplicity, we explain the theory of Radon transform in 2D cases, which represents a slice through the 3D object.

The formulation of a line integral through an object, represented by the function $f(x, y)$, is given for the parameters θ and r [27]. These parameters define the line $\ell(\theta, r)$ as

$$\ell : x \cos(\theta) + y \sin(\theta) = r, \tag{2.1}$$

where θ is the rotation angle, r is the distance from the line to the center of the object. This is illustrated in Figure 2.1. The line integral along such a line is the

then defined as

$$p(\theta, r) = p(\theta, x\cos(\theta) + y\sin(\theta)) = \int_{\ell(\theta, r)} f(x, y)d\ell = Rf(x, y). \qquad (2.2)$$

Here, we use R to represent the Radon transform function that maps 2D object $f(x, y)$ into its projection at rotation angle θ as $p(\theta, r)$ as shown in Figure 2.1. In this way, the Radon transform maps data from its real space representation in (x, y)-coordinates to its Radon transform in (θ, r)-coordinates. In the case of electron tomography, we assume to use transmission electron microscope to provide such parallel projections, which is a good approximation in the experiment. In parallel projections, the source and detector have the same size, and each projection consists of line integrals at a constant θ with several values for r. Several other types of projections exist like fan-beam or cone-beam projections, but as they are of no relevance for electron tomography, only parallel projections are considered [28].
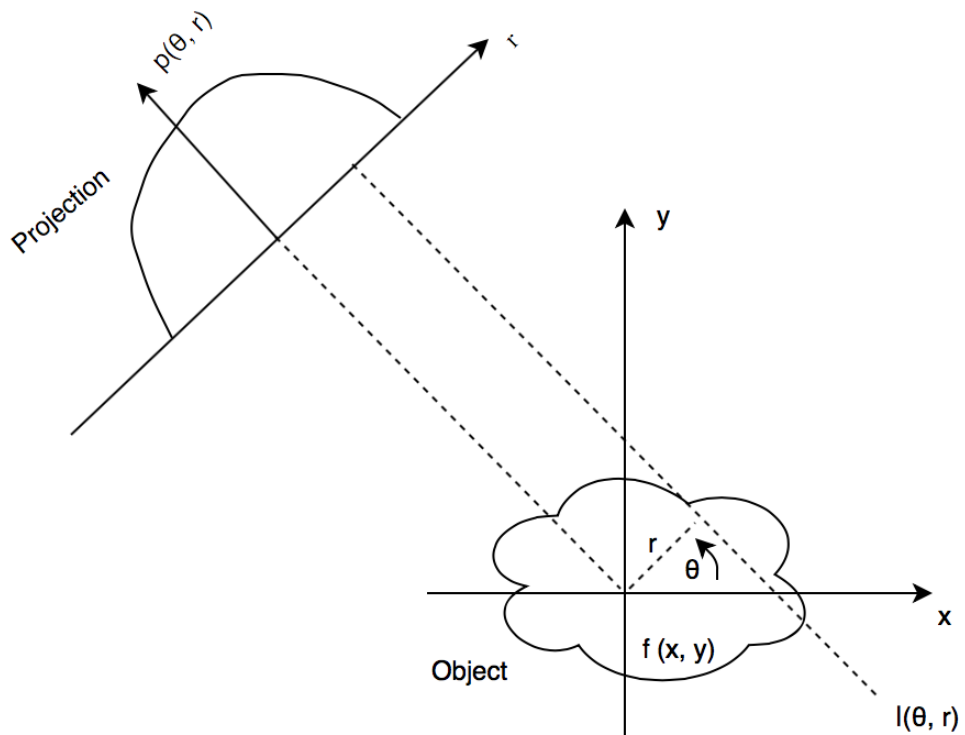
Figure 2.1 *The Radon Transform in 2D case*

With the help of Radom transform, the projections are formed as by calculating the
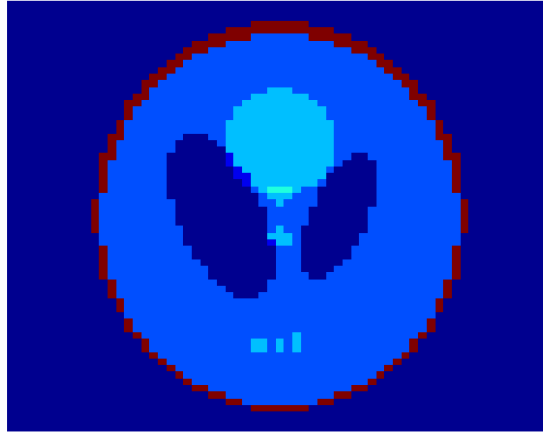
(a) The modified Shepp-Logan phantom
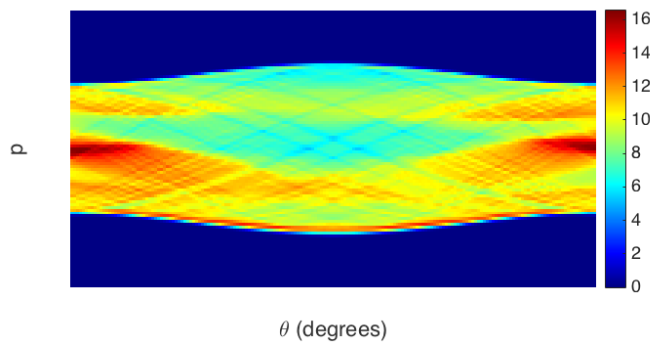
(b) The sinogram of modified Shepp-Logan phantom

Figure *2.2 The Radon transform for modified Shepp-Logan phantom*

line integrals of object from certain angle range. By rotating the object or TEM, we get a collection of several projections at different rotation angles. As we see in Figure 2.2, Figure 2.2(a) shows the modified Shepp-Logan phantom in 2D and Figure 2.2(b) is the sinogram that shows the projections along all projection angles. Sinogram represents the raw data available for electron tomography reconstruction [29]. Since θ and r are two arguments that represent projection at certain angle, they are also vertical and horizontal axes respectively in the sinogram. Whereas, the situation is different in 3D case. Since the projections are 2D images for a volume, it is not eacy to observe all the projections in one figure like Figure 2.2(b). In Figure 2.3, we only show three projections out of M projections (M is the total number of projections). To see inside the volume, the corss section figures are also given.
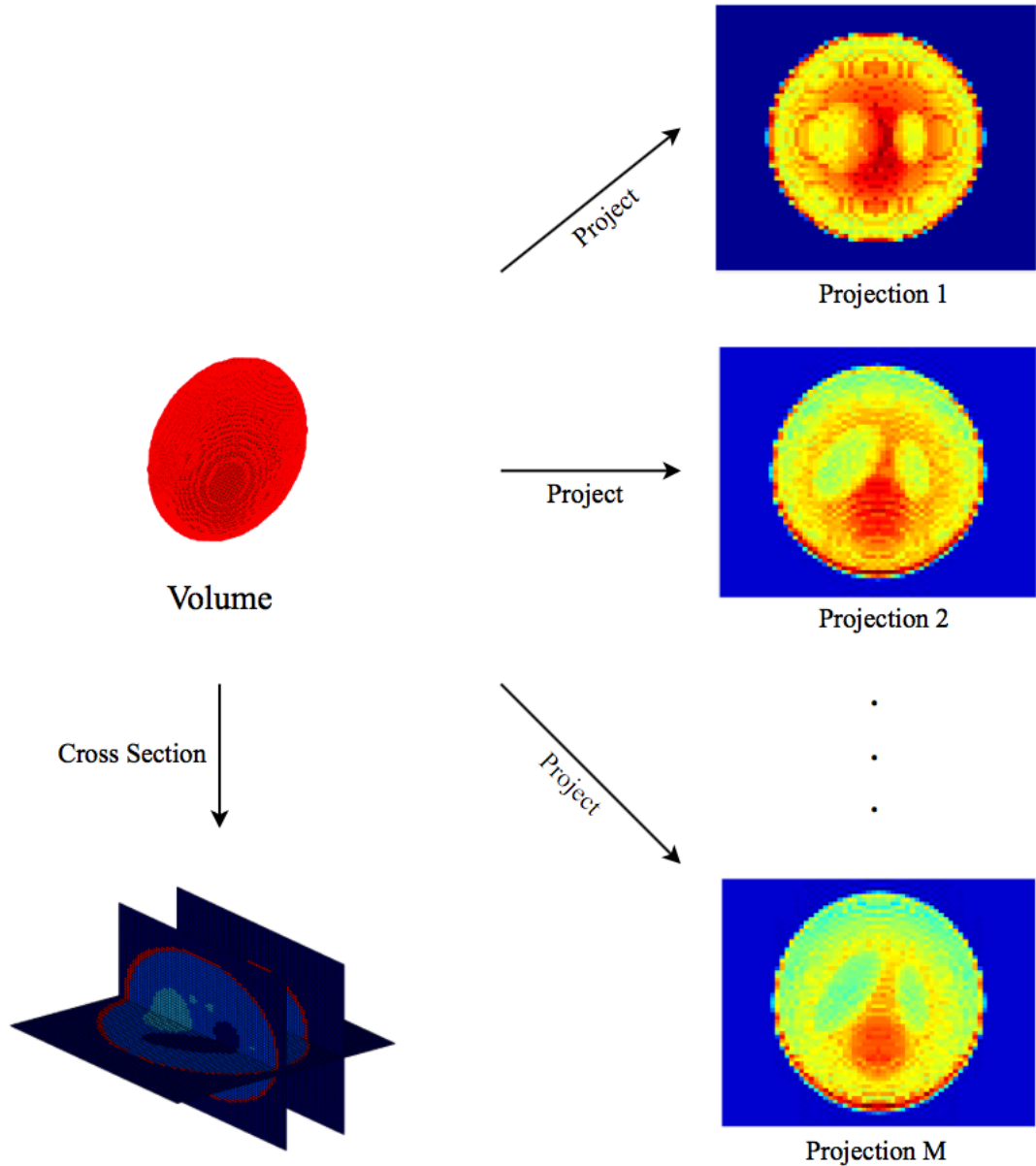
Figure 2.3 *The 3D projection in 3D case. The volume is Shepp-Logan phantom.*

2.2   Plain Back-Projection

As we explain in section 2.1, the Radon transform maps a 2D object $f(x,y)$ into a sinogram $p(\theta, r)$ consisting of line integrals through the object. So that the reconstruction problem becomes how to reconstruct the object by using its raw data. One approach, simple back-projection takes each sinogram value and smears it back

into object space along the corresponding line,

$$f_b(x, y) = \int_0^\pi p(\theta, x\cos(\theta) + y\sin(\theta))d\theta. \qquad (2.3)$$

Unfortunately in its simplest form this procedure does not recover the object $f(x, y)$, but instead yields a blurred version of the object $f_b(x, y)$ [26]. This blurred version $f_b(x, y)$ is called a layergram , as illustrated in Figure 2.4.
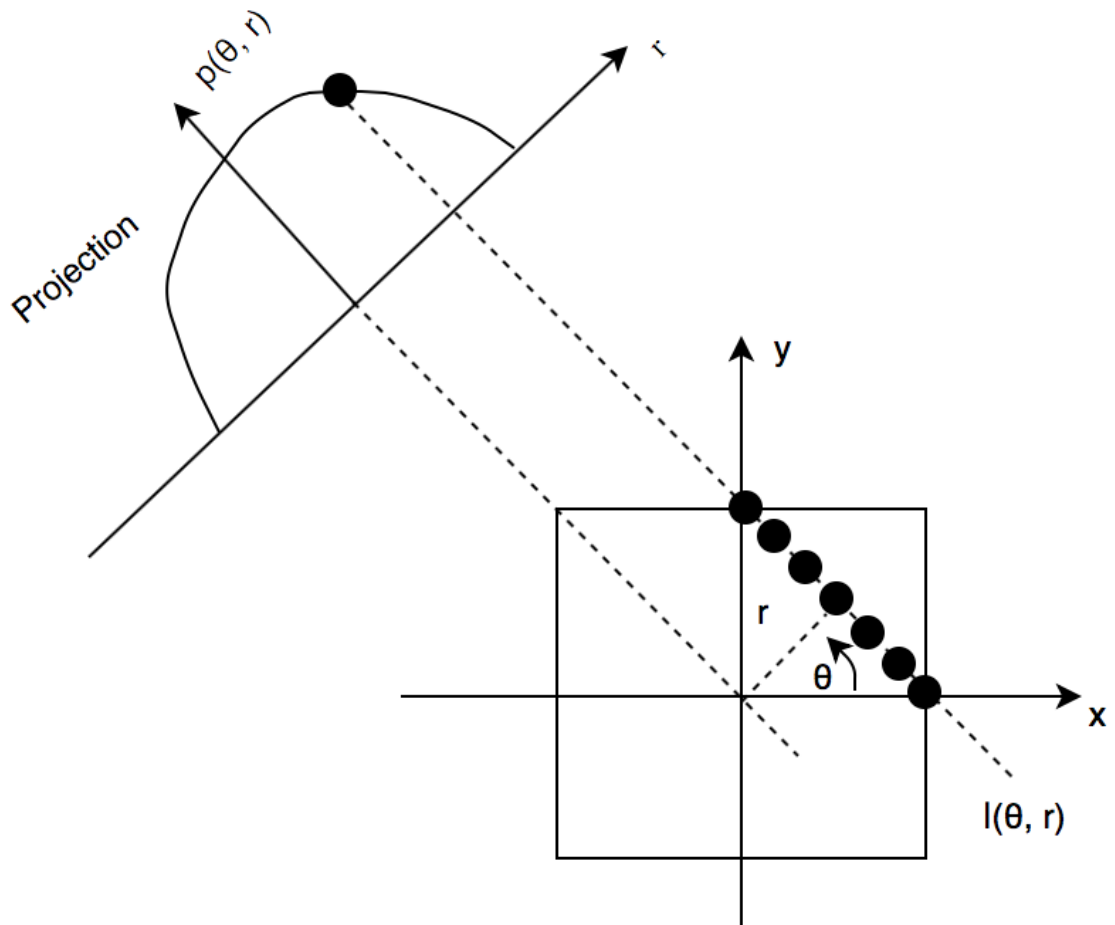
Figure *2.4* *The process of plain back-projection*

2.3   Fourier Slice Theorem

The Fourier slice theorem explores the principle of Radon transform in Frequency domain, rather than image domain as shown in 2.3. It gives a relationship between

the Radon transform and the Fourier transform of an object and has great impor-
tance for all reconstruction procedures [30, 31]. To explain Fourier slice theorem,
we employ two-dimensional Fourier transform to an object $f(x, y)$,

$$F(u, v) = \int_{-\infty}^{\infty} \int_{-\infty}^{\infty} f(x, y)e^{-j2\pi(ux+uy)} \, dxdy. \tag{2.4}$$

On the other hand, we take a look at the Fourier transform of projection $p(\theta, r)$,

$$P(\theta, w) = \int_{-\infty}^{\infty} p(\theta, r)e^{-j2\pi wr} dr. \tag{2.5}$$

Combining equation 2.1, 2.4 and 2.5, the Fourier-slice theorem that shows the
Fourier transform of a projection at an angle θ is equal to a central slice through
the 2D Fourier transform of the object. Its methermatical notation is

$$P(\theta, w) = F(wcos\theta, wsin\theta). \tag{2.6}$$

Figure 2.5 shows that, one projection at projection angle θ is one slice at Fourier
space after Fourier transform. If we take Fourier transform of all the projection
data, their samples in Fourier space is shown in the left side of Figure 2.6.

Figure **2.5** *One project data in 2D corresponds to a slice in Fourier space*

In this way, projections acquired at different tilt angles give information about the
Fourier transform of the object along central slices. If we have enough raw data, then
the full information about the object can be recovered. From these considerations,

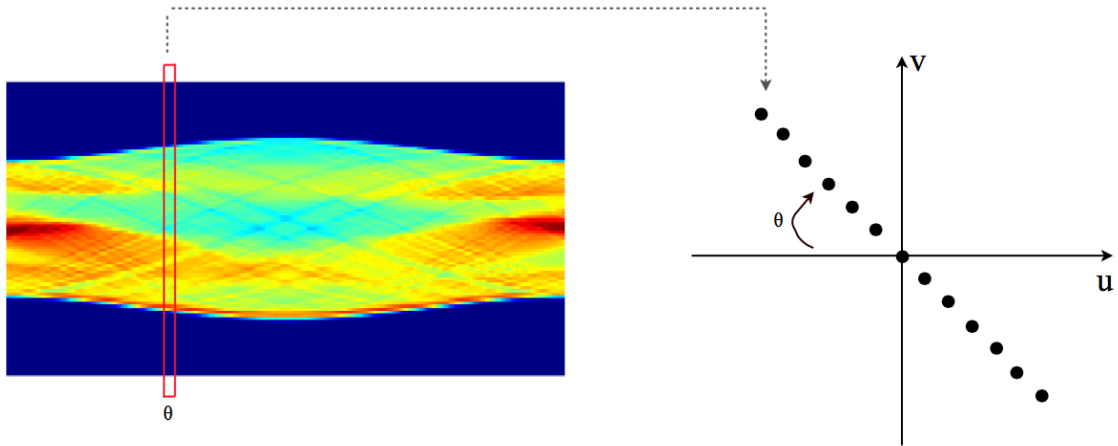we could find a way of theoretically reconstructing the object by inverse Fourier transform in two dimensions. Such method is known as direct Fourier reconstruction method [32]. However, this method requires an interpolation in Fourier space to transform the discrete data from polar coordinates to Cartesian coordinates, which may introduce inaccuracy during reconstruction. It is therefore generally preferred to reformulate the problem in a way that it requires an interpolation in real space rather than in Fourier space.
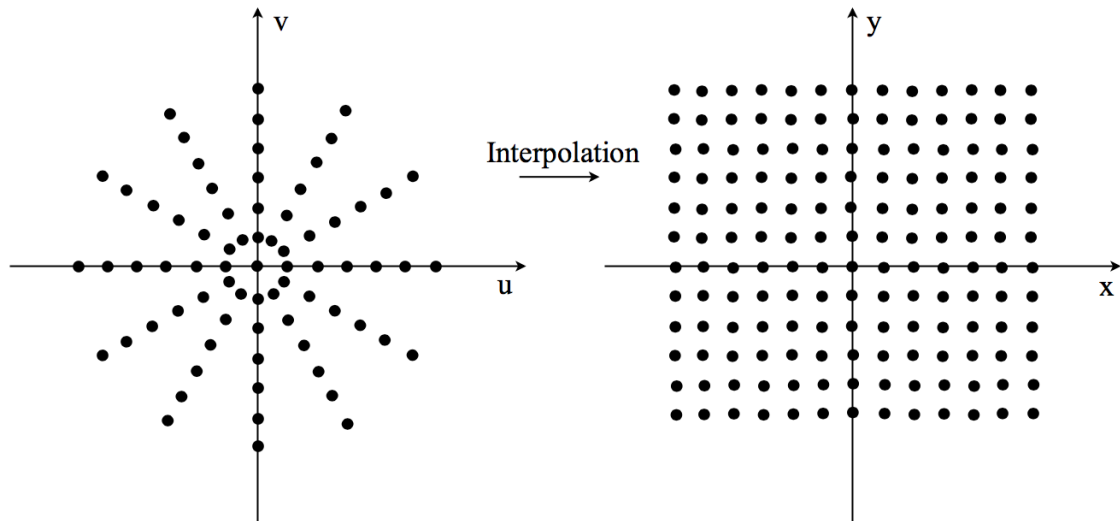
Figure 2.6 *The interpolation error from frequency domain to image domain*

In Figure 2.6, we observe that the Fourier space filled by samples is denser at low frequencies and sparser at high frequencies. It means that we should apply a scalable operation to those data. Otherwise, the low-frequency information of the object is overemphasized compared to the high-frequency information. Nowadays, the solution to the linear inverse problem is either computed by applying a carefully designed weighted adjoint operator, such as weighted backprojection (WBP) that addresses the non-uniform sampling, or by using an iterative approach for inversion [16].

2.4   Weighted Back-Projection

By using inverse Fourier transform and polar coordinates, the object $f(x, y)$ can be reconstructed as

$$f(x,y) = \int_0^{2\pi} \int_{-\infty}^{\infty} F(\theta, r) r e^{j2\pi wt} dr d\theta, \tag{2.7}$$

r has been defined previously in equation 2.1. This is the basic formula for the weighted backprojection (WBP). To see how to equalize the impact of different frequency components, we split this procedure into two parts. At first, the Fourier transform of projection is filtered in Fourier space by a ramp filter $|w|$ resulting the filtered projection $Q(\theta, r)$:

$$Q(\theta, r) = \int_{-\infty}^{\infty} P(\theta, w)|w|e^{j2\pi wt}dt. \tag{2.8}$$

Ramp-filer is a decent choice of the weighting function that correct this impact effectively. Without this designed filter, the inverse procedure will directly transfer the dense sampling in to the central part of the Fourier domain to the reconstruction [33]. Because of the overestimated low-frequency samples, the resulting reconstruction is the blurred version of the ground truth.

After filtering, we back-project the filtered projection as

$$f(x, y) = \int_{0}^{\pi} Q(\theta, xcos(\theta) + ysin(\theta))d\theta \tag{2.9}$$

This operation is similar as 2.3, the main difference is that $Q(\theta, xcos(\theta) + ysin(\theta))$ is the filtered version of projections in frequency domain, instead of original projections. In the back-projection operation, the filtered projections for all angles are integrated to reconstruct an estimate of the original object $f(x, y)$. Each filtered projection will contribute equally to all points, which are on lines through the object in the direction of projection. Although we get the mathematical expression

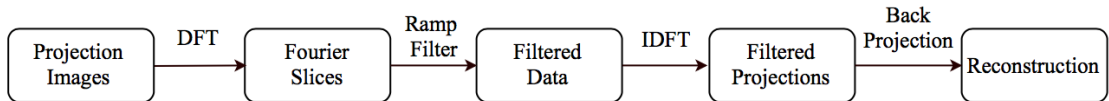**Figure 2.7** *The process of weighted back-projection algorithm*

of filtered back-projection for continuous signals, this expression should be adapted for practical cases where discrete signals are customary. Besides, the projections would not be noiseless in practice. To overcome the noisy problem in projections, we should improve the filter to reduce high-frequency noise, which is a complicated procedure.

2.5 Simultaneous Iterative Reconstruction Method

Though the ground truth cannot be accurately constructed by merely using simple back-projection (SBP) operation, we could combine it with iterative reconstruction algorithms. Iterative algorithms are equilavent to algebraic reconstruction technique (ART). Specifically, we get the initial reconstruction from back-projection operation, which is a stronger weighting of low-frequency components. Then the initial reconstruction will be improved iteratively by using high-frequency contributions up to the amount of available data.

Simultaneous iterative reconstruction technique (SIRT) is one of those iterative reconstruction methods based on simple back-projection (SBP) algorithm. At the beginning, the sinogram is back-projected using SBP, resulting the experimental layergram $f_b^0(x, y)$. At iteration k-1, the reconstructed image $f_b^{k-1}(x, y)$ is re-projected and reconstructed as $R^T R f_b^{k-1}(x, y)$. By taking the difference between $R^T R f_b^{k-1}(x, y)$ and layergram $f_b^0(x, y)$, this update value is added to the reconstructed image $f_b^{k-1}(x, y)$ constitute a new image $f_b^k(x, y)$,

$$f_b^k(x, y) = f_b^{k-1}(x, y) - \lambda(R^T R f_b^{k-1}(x, y) - f_b^0(x, y)), \tag{2.10}$$

Recall R represents the Radon transform, R^T is the SBP procedure and λ is the update parameter. With a suitable choice of λ, this procedure is performed sequentially until it reaches an adequate solution. A criterion for the optimal number of iterations was proposed in [34].
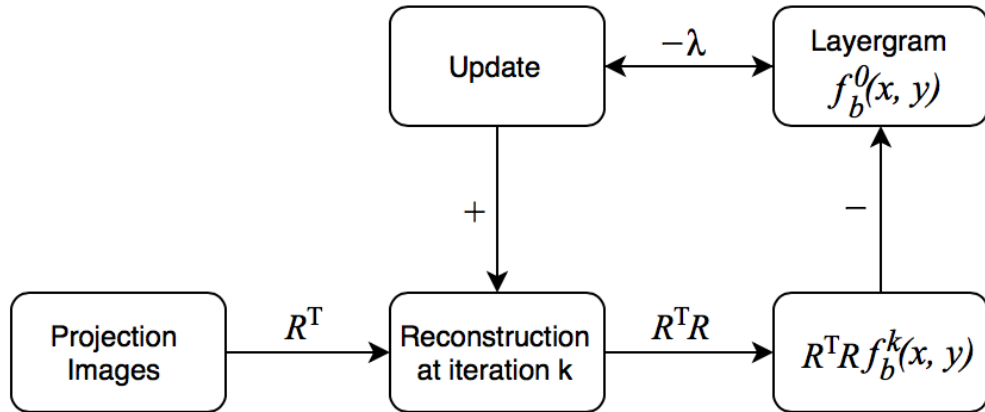

Figure 2.8 *The schematic overview of the SIRT algorithm*

2.6 Fourier-based Iterative Reconstruction Method

Fourier-based iterative reconstruction method (FIRM) is another iterative reconstruction approach that implements both projection and backprojection in Fourier space by using non-uniform fast Fourier transform (NUFFT). By exploiting the Toeplitz structure of projection and backprojection operators, FIRM is considerably faster than those of traditional iterative algebraic approaches [16].

2.6.1 Non-Uniform Fast Fourier Transform

Discrete Fourier transform (DFT) converts an image from image domain to the frequency domain. Because the pixel values in the image domain are equally spaced, so that those sample values in frequency domain are equally distributed as well. Consider a square image $f(x, y)$ with size $N \times N$, its two-dimensional DFT is

$$F(u, v) = \sum_{x=\frac{-(N-1)}{2}}^{\frac{(N-1)}{2}} \sum_{y=\frac{-(N-1)}{2}}^{\frac{(N-1)}{2}} f(x, y) e^{-j2\pi(ux+vy)/N}, \qquad (2.11)$$

where u and v are the coordinates in frequancy domain. In equation 2.11, both image samples and frequency samples are uniform in the range from $\frac{-(N-1)}{2}$ to $\frac{(N-1)}{2}$.

However, as we analyze in section 2.3, those frequency samples cannot be equally-distributed. Instead of locating at (u, v) which defined in equation 2.11, the samples in the frequency domain site at (t_x, t_y), where both t_x and t_y are arbitrary numbers. As a result, the intervals of different samples are irregular,

$$F(u, v) = \sum_{x=\frac{-(N-1)}{2}}^{\frac{(N-1)}{2}} \sum_{y=\frac{-(N-1)}{2}}^{\frac{(N-1)}{2}} f(x, y) e^{-j2\pi(ut_x+vt_y)/N}. \qquad (2.12)$$

To process the non-uniformly distributed samples in the frequency domain, fast Fourier transform (FFT) is not good enough. However, we could interpolate an oversampled FFT that approximates the procedure of equation 2.12, this method is called non-uniform fast Fourier transform (NUFFT). The widely used interpolation method is the min-max interpolation [35], which is quite efficient.

2.6.2 Reconstruction Approach

As the key procedure of Fourier-based reconstruction method, NUFFT solves the problem of efficiently manipulating image data between the frequency domain and the image domain. Given a volume of size $N \times N \times N$, one of its projection along $z-$axis $P_R(x, y)$ is

$$P_R(x, y) = \int_{-\infty}^{\infty} \mathbf{V}_R(x, y, z)dz, \tag{2.13}$$

where $\mathbf{V}_R$ is the volume rotated by using rotation matrix R. Recall the Fourier slice theorem in section 2.3, the 2D Fourier transform of a projection image equals to one center slice of the 3D Fourier transform of the volume. By using FFT on both sides of equation 2.13, the Fourier slice theorem shows that [36]

$$\mathscr{F}P_R(u, v) = \mathscr{F}\mathbf{V}_R(x, y, 0). \tag{2.14}$$

Instead of the continuous signal, the volume $\mathbf{V}$ is sampled on a Cartesian grid $\{\mathbf{n} : \mathbf{n} \in Z^3, -N/2 \leq \mathbf{n} < N/2\}$ in practice. Assume there are M projection angles, each of them corresponds to a rotation matrix R_m, $m \in \{1, ..., M\}$, so that there will be M projection images as well. After taking the discrete Fourier transform of equation 2.14, one central slice corresponding to m^{th} projection angle is [16]

$$S_m = P(V_{R_m}) = \sum_{\mathbf{n}} \mathbf{V}exp(-j \cdot \langle \mathbf{n}, R_m^{-1}(w_u, w_v, 0) \rangle). \tag{2.15}$$

Here, we use symbol P to represent the forward-projection operator that maps the volume to its projection image in Fourier domain defined by rotation matrix R_m. And $(w_u, w_v) = 2\pi(u, v)/N$, where $u, v \in \mathbb{Z}$, are the Cartesian coordinates of the central slice. As we explained in section 2.6.1, equation 2.15 can be implemented efficiently by using NUFFT. By individually taking the inverse FFT for each central slice S_m, the projection image U_m is:

$$U_m = \mathscr{F}^{-1}S_m. \tag{2.16}$$

Since the operator P directly maps the volume to one of its central slice, part of the volume can be reconstructed by the inverse operator P^{-1} using inverse NUFFT,

$$P^{-1}(S_m) = \sum_{\mathbf{n}} S_m exp(j \cdot \langle \mathbf{n}, R_m^{-1}(w_u, w_v, 0) \rangle). \tag{2.17}$$

So that the reconstructed volume is the sum of the result in equation 2.17 for every rotation matrix R_m,

$$\mathbf{V}^* = \sum_{m=1}^{M} P^{-1}S_m. = P^{-1}S. \tag{2.18}$$

Since the summation $\sum$ does not affect the calculation of back-projection operation and can be included into operation P^{-1}, we use $S = \{S_1, S_2, ..., S_M\}$ to represent the stack of Fourier slices. So that the inverse operator P^{-1} equals to the back-projection operation in electron tomography, and the reconstruction process is simplified as

$$\mathbf{V}^* = P^{-1}P\mathbf{V} \tag{2.19}$$

So far, the reconstruction process is direct Fourier reconstruction[37, 32] using NUFFT. Besides, the image acquisition part would not be so ideal in practice. There are always errors in the projection images, that is

$$S = P\mathbf{V} + \mathbf{e}, \tag{2.20}$$

where $\mathbf{e}$ could be noise or projection angle error. Thus the key problem is minimizing the effect of error term $\mathbf{e}$ during the reconstruction process. This would be easily expressed as traditional least squares function in signal processing [38]:

$$\text{minimize} \quad \varepsilon = \|S - P\mathbf{V}\|^2. \tag{2.21}$$

If the cost function ε converge to 0, the volume $\mathbf{V}^*$ reconstructed from the Fourier slices S using equation 2.18 would be more similar to original volume $\mathbf{V}$.

2.6.3 Conjugate Gradient Method

Conjugate gradient (CG) is a numerical solution for minimazing equation 2.21. By setting $\varepsilon = 0$, the analytical solution to this least-squares cost function is known as normal equation:

$$P^{-1}P\mathbf{V} = P^{-1}S. \tag{2.22}$$

Since $P^{-1}P = Q$ is symmetric positive-semidefinite [16], conjugate gradient could be an useful tool to iteratively find the minimizer for equation 2.21. And the whole process of conjugate gradient is shown in Figure 2.9. Specially, each step of iteration loop is [39]:
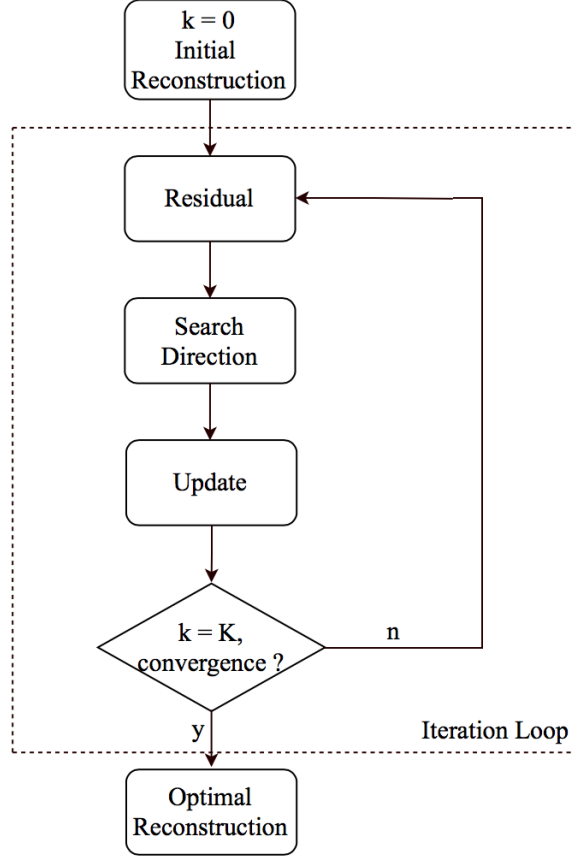
Figure 2.9 *The process of conjugate gradient*

1. Set initial residual $\mathbf{r}_0 = \mathbf{V}^* - P^{-1}P\mathbf{V}^0$ and initial search direction $\boldsymbol{\alpha}_0 = \mathbf{r}_0$, where $\mathbf{V}^0$ is the initial guess and could be all zero at the beginning of iteration.

2. For iteration k = 0 to K:

   (a) Calculate the scalar $p_k = \frac{\mathbf{r}_k^T \mathbf{r}_k}{\boldsymbol{\alpha}_k^T A \boldsymbol{\alpha}_k}$.

   (b) Update reconstructed volume $\mathbf{V}^{k+1} = \mathbf{V}^k + \boldsymbol{\alpha}_k p_k$.

   (c) Update the residual for next iteration $\mathbf{r}_{k+1} = \mathbf{r}_k - p_k P^{-1} P \boldsymbol{\alpha}_k$.

   (d) Get the scalar for search direction $\beta_k = \frac{\mathbf{r}_{k+1}^T \mathbf{r}_{k+1}}{\mathbf{r}_k^T \mathbf{r}_k}$.

   (e) Update search direction for next iteration $\boldsymbol{\alpha}_{k+1} = \mathbf{r}_{k+1} + \beta_k \boldsymbol{\alpha}_k$.

3. The iteration stops when maximum number of iteration is reached or no further decrease of cost function is observed. The resulting volume $\mathbf{V}^k$ is the optimal solution.
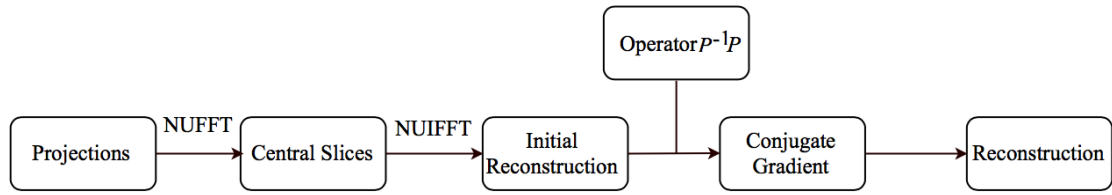
Figure   2.10 *The whole process of FIRM.*

In Figure 2.10, we give the process of FIRM combining with conjugate gradient method. For FIRM, the operation $P^{-1}P$ is the composition of the backward projection and forward projection in frequency domain. Unlike SIRT where the projection and back-projection are applied to the result at each iteration, FIRM procomputes $P^{-1}P$ using the non-uniform fast Fourier transform and efficiently applies it in conjugate gradient method. Due to the Toeplitz structure of $P^{-1}P$, the iteration speed is faster than traditional iterative reconstruction method [16]. Figure 2.11 shows the performance of FIRM on ideal projection data, we see the residual norm declines sharply in early ten iterations and towards zero afterward.
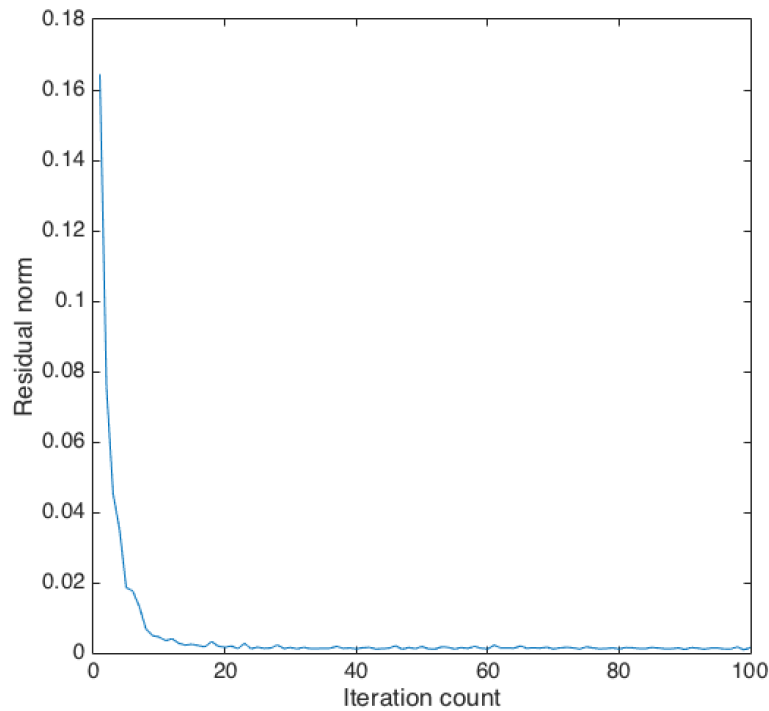

Figure   2.11 *The plot of residual norm vesus iteration count for FIRM. Except SNR = 100, any other types of errors are not introduced in projection images.*

3. 3D ALIGNMENT

This chapter introduces alignment methods that complete registration process for the EM tilt-series. To align projection images, we need to compute the projection geometry of the tilt series. After that, we rectify the deviations from the assumed ideal projection geometry using simple 2D geometric transformations for the images before computing a tomographic reconstruction. When acquiring the images at the different tilt angles, the specimen is tracked into the field of view at each angle, which results in possible local shifts between the various images. The alignment methods we introduce in this chapter minimize the effect of such geometry shifts. At first, we present an useful method of image alignment, marker-based alignment. This method tracks the measured coordinates of fiducial markers in the series of images and then fits them to equations that describe the image projection [40]. Then, we give the principle of an alternative method that bases on cross-correlation of the successive projection images. However, due to the inefficiency or inaccuracy in the previous two methods, feature-based alignment method and refinement method are studied since 2001. The feature-based alignment needs to explore embeded discriminable features in the projection images by using computer vision algorithms and then use these features for alignment. However, these features are treated as another form of the marker in alignment problem. In addition to the computational inefficieny in detect features, feature-based alignment method has the same disadvatanges in marker-based alignment method. A more powerful way to solve alignment problem is refinement method. the alignment problem can be seen as an optimization problem that could be solved in a refinement way.

3.1 Marker-based Alignment Method

For marker-based alignment method, a certain number of high contrast fiducial markers should be set in the projected 3D volume. With their high contrast, these fiducial markers are assumed to be immobile with respect to the volume during

tilt-series acquisition. In this way, the coordinates of those fiducial markers in the projection images are used as the references. The position changes of those fiducial markers also imply the orientation changes during projection.

The fiducial marker tracking alignment requires that markers are added to the sample. The alignment is then done by measuring the coordinates of the fiducial markers through the entire tilt series.The commonly used markers are gold particles with high contrast. The markers are assumed to be immobile with respect to the sample, and thus a change in position of the markers implies movement of the sample. Figure 3.1 shows the usage of fiducial markers in tilt series. The geometric parameters required to align the images are derived from the measured projected positions of the markers using least squares method. For the ith fiducial marker $\mathbf{m}_i = (x_i, y_i, z_i)$, where x_i, y_i, z_i are the coordinates in the volume. Given the jth orientation parameter $(\phi_j, \theta_j, \psi_j)$ (defined in section 4.1.1), we define the measured coordinates of this fiducial marker in the projection image.

$$\mathbf{p}_{ij} = (u_{ij}, v_{ij}) = A_j \mathbf{m}_i, \tag{3.1}$$

where A_j is an affine mapping at orientation angle $(\phi_j, \theta_j, \psi_j)$, which maps the fiducial marker from 3D coordinate system (orginal volume) into 2D image plane (the projection plane). However, if there are orientation errors during projection acquisition, the noisy orientation parameter $(\phi_j^*, \theta_j^*, \psi_j^*)$ cause the actually projected coordinates of the fiducial markers change as well, the resulting noisy coordinates are

$$\mathbf{p}_{ij}^* = (u_{ij}^*, v_{ij}^*) = A_j^* \mathbf{m}_i \tag{3.2}$$

In this way, aligning the tilt-series is equivalent to find a solution that minimize the error function, which is the sum of squares error between measured and projected coordinates for all the fiducial markers:

$$\text{minimize} \quad \sum_i \sum_j ((u_{ij} - u_{ij}^*)^2 + (v_{ij} - v_{ij}^*)^2). \tag{3.3}$$

To find unique solution for equation 3.3, we need to constrain equation 3.1 and equation 3.2 by setting all variables except the rotation angles after projection as constant value on one view [41].

Besides the computational burden in finding unique solution for above equations, marker-based method lacks an universal way to set appropriate distributed mark-
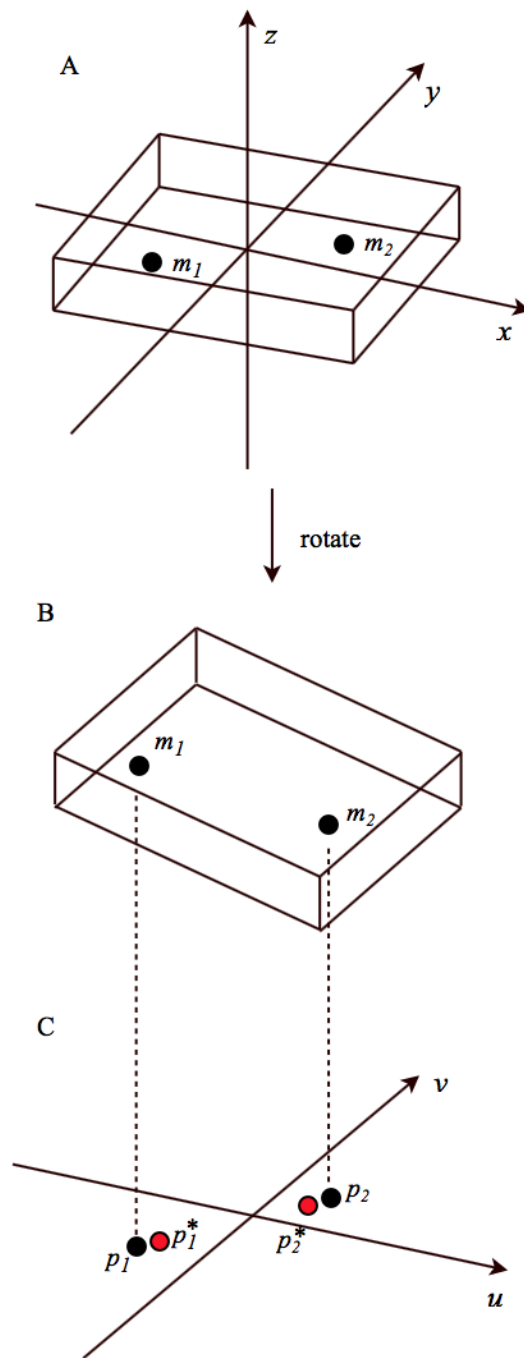
Figure 3.1 *(A) Two fiducial markers m_1 and m_2 in a volume of 3D coordinte system (x, y, z). (B) Rotating the volume at certain angle (ϕ, θ, ψ). (C) The fiducial markers in projection space (u, v). Black represents the predefined location for the markers. Red markers are noisy locations resulting from miss-alignment.*

ers for different specimens. Setting appropriate distributed markers and tracking their posission accurately are labor-intensive steps. Meanwhile, those high contrast markers may introduce artifacts during back-projection reconstruction.

3.2 Cross-Correlation Alignment Method

Cross-correlation-based method computes the translational alignment for successive tilt series. For electron tomography, the projection images of a tilt series represent different aspects of the 3D structure. The successive projection images do not differ too much in an ideal situation. This method defines a discrete 2D cross-correlation function $f(m, n)$ between two neighboring projections images U_1 and U_2:

$$f(m, n) = \frac{1}{MN} \sum_{i}^{M-1} \sum_{j}^{N-1} U_1(i, j) U_2(i + m, j + n), \tag{3.4}$$

where M and N denote the number of pixels in horizontal and vertical direction for these projection images. In this way, the alignment procedure is finding a shift (m_0, n_0), so that function $f(m_0, n_0)$ reaches its maximum value among all available shifts. Since the two projection images are acquired at different tilt angles, the correlation will not coincide entirely. However, finding the peak correlation value is equivalent to estimate the relative shift parameters. Once we get the estimations of relative shift for a sufficient number of tilt series, we could align the images by translating the images with those negative shift values. Moreover, the calculation of correlation function would be more efficient in frequency domain by using FFT and IFFT:

$$f(m, n) = \mathscr{F}^{-1}[\mathscr{F}U_1(i, j) \cdot \mathscr{F}U_2(i + m, j + n)] \tag{3.5}$$

From the above analysis, the cross-correlation is straightforward to implement as shown in Figure 3.2. However, a commonly used way to find such peak correlation value is through exhausive searching, which is computationally expensive. Besides, only two successive projection images are considered in calculating the shift parameter at each time. Although this procedure will continue sequentially for all the projection images, the error will accumulate for each pair of projection images, this phenomenon is called error propagation. Besides, cross-correlation focuses on 2D plane alignment rather than 3D motion that may occur in practice.
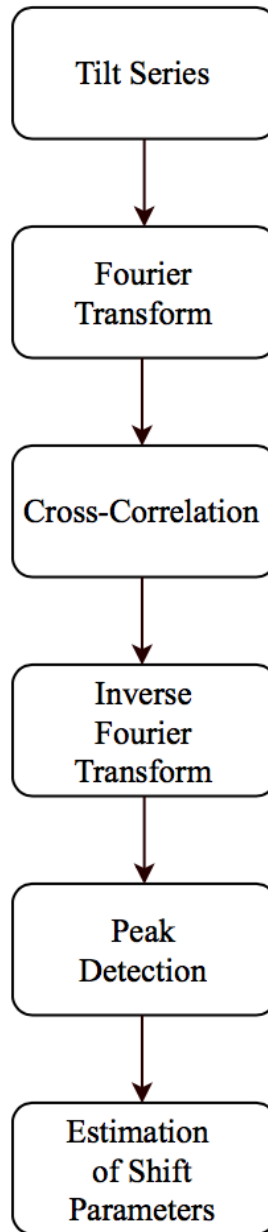
Figure 3.2 *The process of cross-correlation alignment*

3.3 Refinement Method

Traditional alignment methods mentioned in previous sections try to solve the motion parameters before the reconstruction procedure. In this section, we discuss a more novel approach that considers alignment together with reconstruction as an optimization problem and then solve them simultaneously by using gradient-based

optimization methods. Recall projection procedure defined in equation 2.15, which maps 3D volume into 2D projection image at the predefined tilt angle (represented as rotation matrix R). To emphasize the relation between orientation angle and miss-alignment, we simplify this equation as

$$U_m = T(\phi_m, \theta_m, \psi_m)\mathbf{V} + \mathbf{e}, \tag{3.6}$$

where $T(\phi_m, \theta_m, \psi_m)$ is the transformation matrix that characterizes how to acquire projection image U_m from the 3D volume $\mathbf{V}$ at m^{th} tilt angle $(\phi_m, \theta_m, \psi_m)$, and $\mathbf{e}$ is the error variable that is introduced when miss alignment happens. In such case, alignment problem is equivalent to minimizing the effect of error variable $\mathbf{e}$. By employing least-squares error rule, the alignment problem becomes an optimization problem for M projection images $U_i, i = 1, 2, ..., M$:

$$\min_{V_\mathbf{n}, \phi_i, \theta_i, \psi_i} \rho(V_\mathbf{n}, \phi_i, \theta_i, \psi_i) = \frac{1}{2}\sum_{i=1}^{M} \|T(\phi_i, \theta_i, \psi_i)\mathbf{V} - U_i\|^2. \tag{3.7}$$

This equation is prevalent in signal processing, and a commonly used way to solve it is the gradient-based algorithm. In this case, the explicit equations for the gradient are hard to derive because of the complexity of transformation matrix T. However, we could use the numerical method to approximate the gradient of this objective function. Recall the differential algebra for a function $f(x)$ is

$$df(x) = \frac{f(x + \Delta x) - f(x)}{\Delta x}. \tag{3.8}$$

Similarily, the partial dericative of $\rho(\mathbf{V}, \phi, \theta, \psi))$ with repect to ϕ_i is:

$$\frac{\partial \rho}{\partial \phi_i} = \frac{T(\phi_i + \Delta\phi, \theta_i, \psi_i) - T(\phi_i, \theta_i\phi_i)}{\Delta\phi}(T(\phi_i, \theta_i\phi_i)\mathbf{V} - U_i). \tag{3.9}$$

By changing the variable in equation 3.9, we could get all the partial derivative of the objective function with respect to the remaining variables $\mathbf{V}, \theta, \psi$ in the same way. Once the gradients are calculated, we get the search direction $\boldsymbol{\alpha}$ for the gradient-based algorithm. If we choose steepest gradient descent, we search for a local minimum of equation 3.7 with the help of the negative of the gradient and some choice of step length η. This procedure fulfills the inequality

$$\rho(x^{(0)} + \eta \cdot \boldsymbol{\alpha}) < \rho(x^{(0)}), \tag{3.10}$$

where $x = (\mathbf{V}, \phi_1, ..., \phi_M, \theta_1, ..., \theta_M, \psi_1, ..., \psi_M)$ is the compound of all the unknown variables contained in objective function 3.7. To avoid finding the local minimum, we could use predefined tilt angles and treat miss-aligned reconstructed volume as a good initial guess of $x^{(0)}$. Following the rule defined in inequality 3.10, new search direction $\boldsymbol{\alpha}^{(k)}$ and step length $\eta^{(k)}$ are computed at k^{th} iteration until there is no further reduction in $\rho(x^{(k)})$. The whole process of refinement is shown in Figure 3.3.
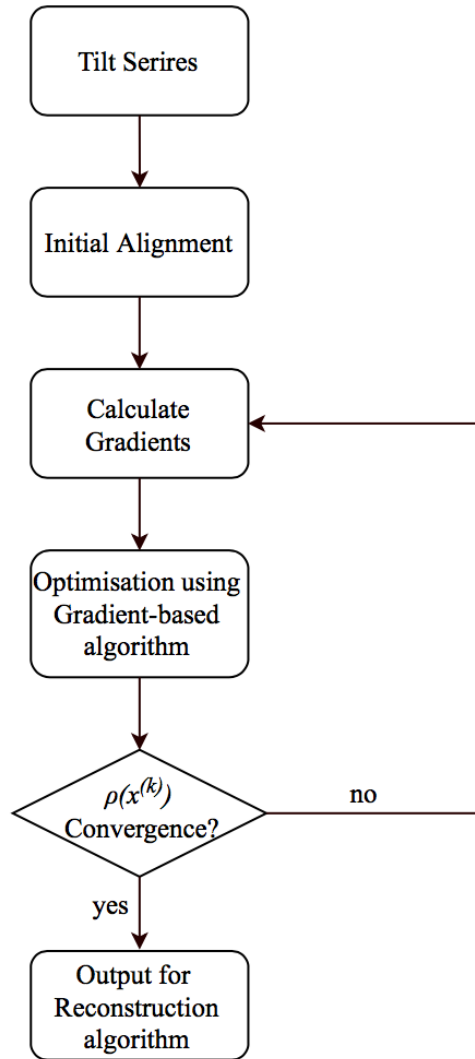

Figure 3.3 *The process of refinement method*

Instead of steepest descent direction, the quasi-Newton scheme can be used to accelerate the convergence of a gradient-based algorithm [22]. Besides, additional prior

information is very helpful in this optimization problem. The other alternative method adds Tikhonov regularizer in the objective function 3.7, which is equivalent to having a Gaussian prior for reconstructed volume $\mathbf{V}$ [19].

4. EXPERIMENTS AND RESULTS

The quality of a 3D reconstruction of an electron tomography experiment relies upon several experimental parameters, such as the maximum achievable tilt range, the number of 2D projections, the alignment of the acquired projections and of course the reconstruction algorithm.

In projection simulation part, 2D projection images are obtained by using NUFFT. During image acquisition, several noise levels and different tilt ranges are introduced. Due to the lack of projection images, the weighted back projection (WBP) reconstruction methods introduce significant artifacts to the reconstruction, which is why they are not applied in this work. Although simultaneous iterative reconstruction technique (SIRT) suffers less in the presence of missing wedge artifacts than the weighted back projection method, it is computationally expensive and hard to get ideal convergence result. So the primary reconstruction method we used in experiment is Fourier-based Iterative reconstruction method (FIRM).

In the quantitative comparison part, we used mean square error (MSE) to measure the quality of reconstruction method under different parameters. Besides, we applied Fourier shell correlation (FSC) to evaluate the resolution of the reconstruction.

4.1   3D Projection Simulation

In this section, the way of obtaining simulated projection images is introduced. The traditional 2D Radom transform is computationally expensive in 3D case. In 3D simulation, a more accurate and scientific projection acquisition method was used. The volume used in this work is the 3D Modified Shepp-Logan phantom. Since Figure2.2(a) shows the 2D Modified Shepp-Logan phantom, Figureonly shows its four slices in 3D case for simplicity.
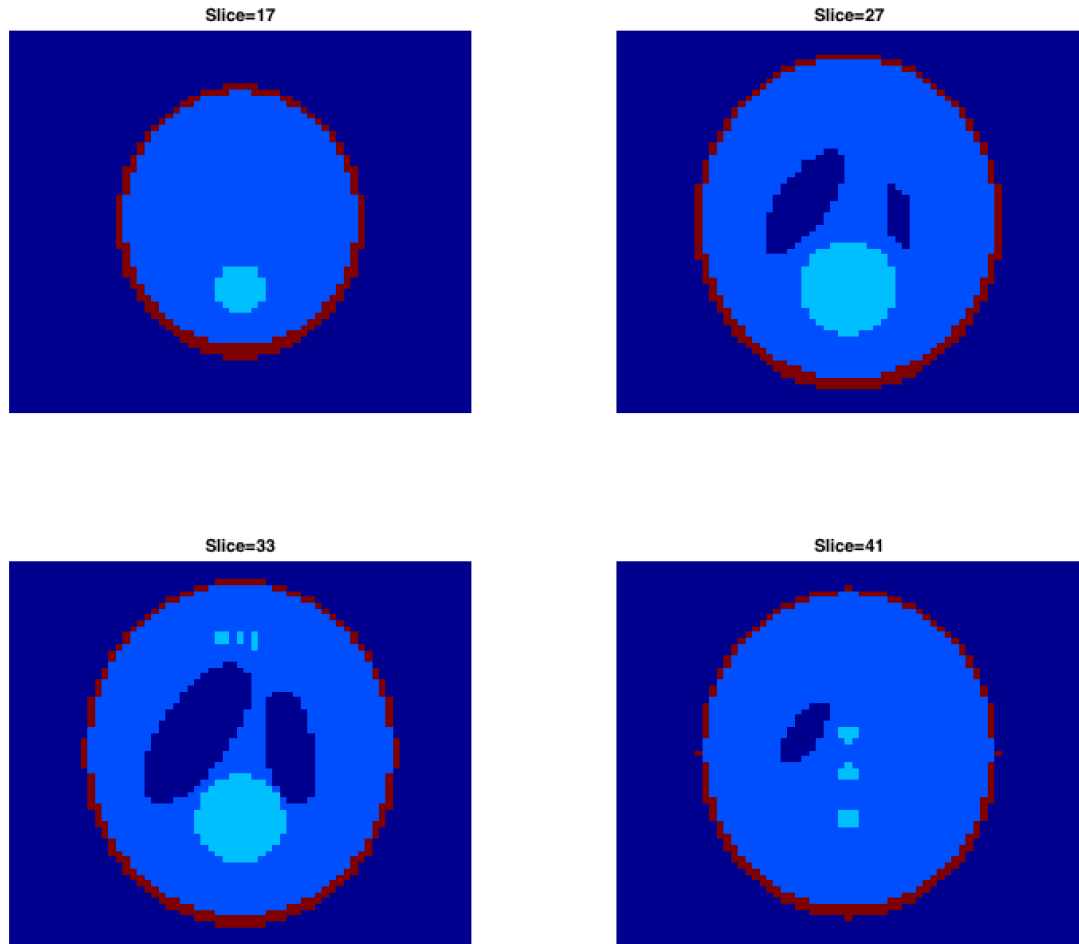
Figure 4.1 *The four slices of 3D Modified Shepp-Logan phantom*

4.1.1   Euler Angle Convention

Euler angle convention is one of the basic concepts in 3D image processing. It uses three parameters that describe orientations in three-dimensional Euclidean space. In electron tomography, Euler angles represent the rotation angles of detected three-dimensional volume during projection acquisition.

Traditionally, the Euler angles in the XYZ convention represent the rotation parameters with respect to the three planes: yz, zx, xy. In electron tomography, ZYZ convention (rotation around the z-axis, followed by a rotation around y, and another around z) is convenient when considering 2D projections of a 3D object [43]. If the Euler angles are (ϕ, θ, ψ), the description of the rotation of a volume would be the
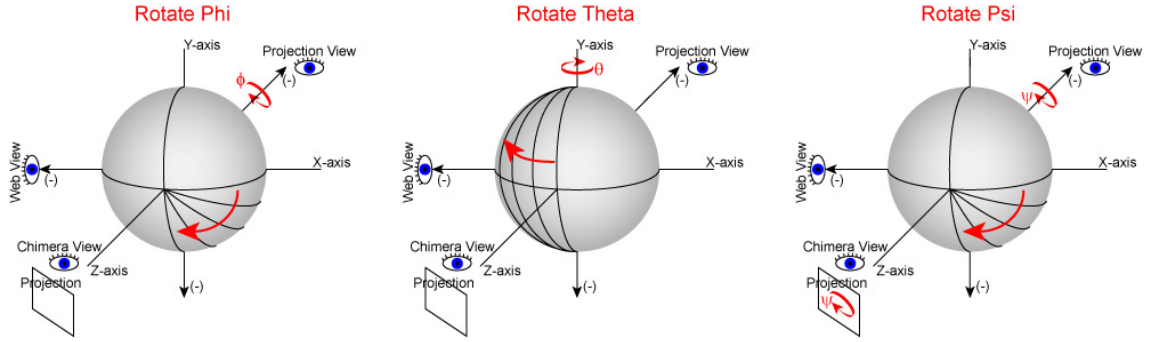
Figure 4.2 *The Euler angles of ZYZ convention [42]*

product of three matrices:

$$R_Z(\psi)R_Y(\theta)R_Z(\phi) =$$
$$\begin{bmatrix} \cos(\psi) & \sin(\psi) & 0 \\ -\sin(\psi) & \cos(\psi) & 0 \\ 0 & 0 & 1 \end{bmatrix} \begin{bmatrix} \cos(\theta) & 0 & -\sin(\theta) \\ 0 & 1 & 0 \\ \sin(\theta) & 0 & \cos(\theta) \end{bmatrix} \begin{bmatrix} \cos(\phi) & \sin(\phi) & 0 \\ -\sin(\phi) & \cos(\phi) & 0 \\ 0 & 0 & 1 \end{bmatrix}. \quad (4.1)$$

As we can see from the equation and figure above, the rightmost matrix is applied first and matrices appear in the order from right to left as clockwise rotations around z, y and z respectively. So that, if a volume $\mathbf{V}$ is rotated according to certain Euler angles (ϕ, θ, ψ), the rotated volume $\mathbf{V}_R$ is expressed as:

$$\mathbf{V}_R = R_Z(\psi)R_Y(\theta)R_Z(\phi)\mathbf{V}. \quad (4.2)$$

4.1.2 Quaternion and Rotation Matrices

Quaternions are useful in calculating three-dimensional rotations in computer graphics. In practical electronic tomography, they can be used alongside Euler angles and rotation matrices,which are needed in projection acquisition and volume reconstruction.

The quaternions $\mathbf{H}$ is a four-dimensional vector space over the real numbers. The unique representation of $\mathbf{H}$ is a linear combination of four basis elements $(\mathbf{1}, i, j, k)$, that is, as $q_r + q_i i + q_j j + q_k k$, where q_r, q_i, q_j, and q_k are real numbers. As a rotation quaternion, $\mathbf{H}$ is an unit quaternion that has unit norm ($\|\mathbf{H}\| = 1$), which provides

a convenient mathematical notation for representing orientations and rotations of objects in three dimensions [44]. According to Euler's rotation theorem [45], the rotation matrix can be represented using the elements of quaternion,

$$R_M = \begin{bmatrix} 1 - 2q_j^2 - 2q_k^2 & 2(q_i q_j + q_k q_r) & 2(q_i q_k - q_j q_r) \\ 2(q_i q_j - q_k q_r) & 1 - 2q_i^2 - 2q_k^2 & 2(q_j q_k + q_i q_r) \\ 2(q_i q_k + q_j q_r) & 2(q_j q_k - q_i q_r) & 1 - 2q_i^2 - 2q_j^2 \end{bmatrix}. \tag{4.3}$$

4.1.3 Parameter Setting

In this work, we introduce three main parameters, the noise level, the tilt range and the variance of projection angle error (VPE) during projection data acquisition.

The Gaussian noise is added into projection images with three different level. We represent nosie level as signal-to-noise (SNR) in images. To see the effect of missing wedge size on the reconstructed image quality, we use four groups of different tilt ranges ($\pm 90°$, $\pm 70°$, $\pm 65°$, $\pm 60°$).

Besides, there is always certain projection angle error during image acquisition. In this experiment, we treat this error as Gaussian distrubuted and use its variance as the quantitive level of the error.

4.2 3D Reconstruction Experiments

We implement both of projection and reconstruction process using MATLAB programming language. In the projection part, the NUFFT package [35] is used to calculate the projection images in frequency domain. After inverse FFT the obtained projection images are shown in Figure 4.3, and the noisy projections are generated by adding white Gaussian noise to these images.

The mainly used reconstruction method in this work is Fourier-based iterative reconstruction method (FIRM). To give a first look at this method, we evaluate its perfromance by using normalized mean-square error (NMSE):

$$NMSE = \left(\frac{\sum(\mathbf{V}_b - \mathbf{V})^2}{\sum \mathbf{V}^2}\right)^{\frac{1}{2}}, \tag{4.4}$$

where $\mathbf{V}$ is the ground truth and $\mathbf{V}_b$ is the reconstructed volume. Given the param-

Projection angle =90   Projection angle =70

Projection angle =65   Projection angle =60
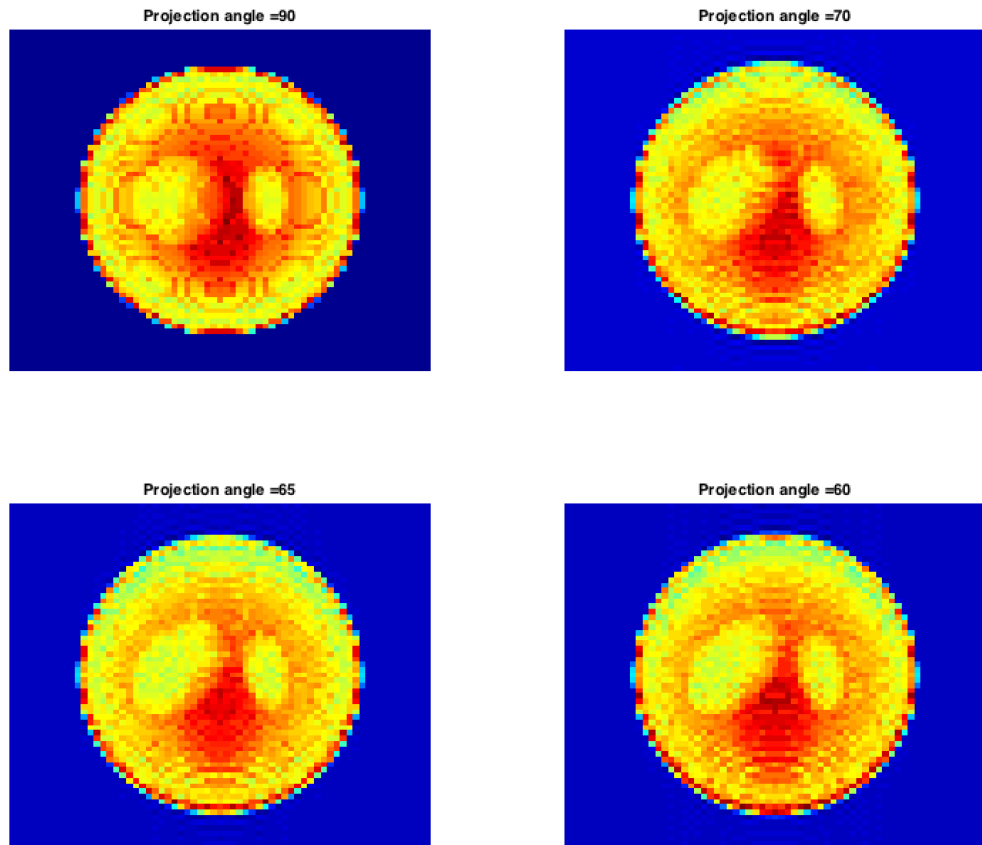
(a) The projection images at four different projection angles without noise

Projection angle =90   Projection angle =70

Projection angle =65   Projection angle =60
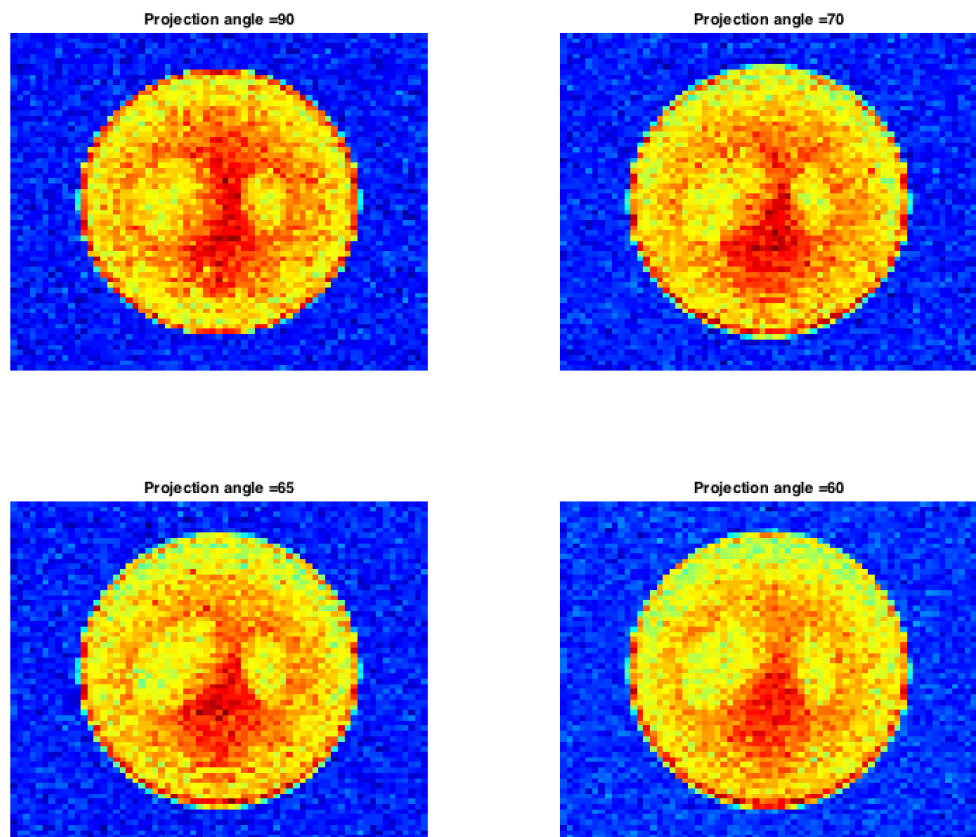
(b) The projection images at four different projection angles when SNR = 50

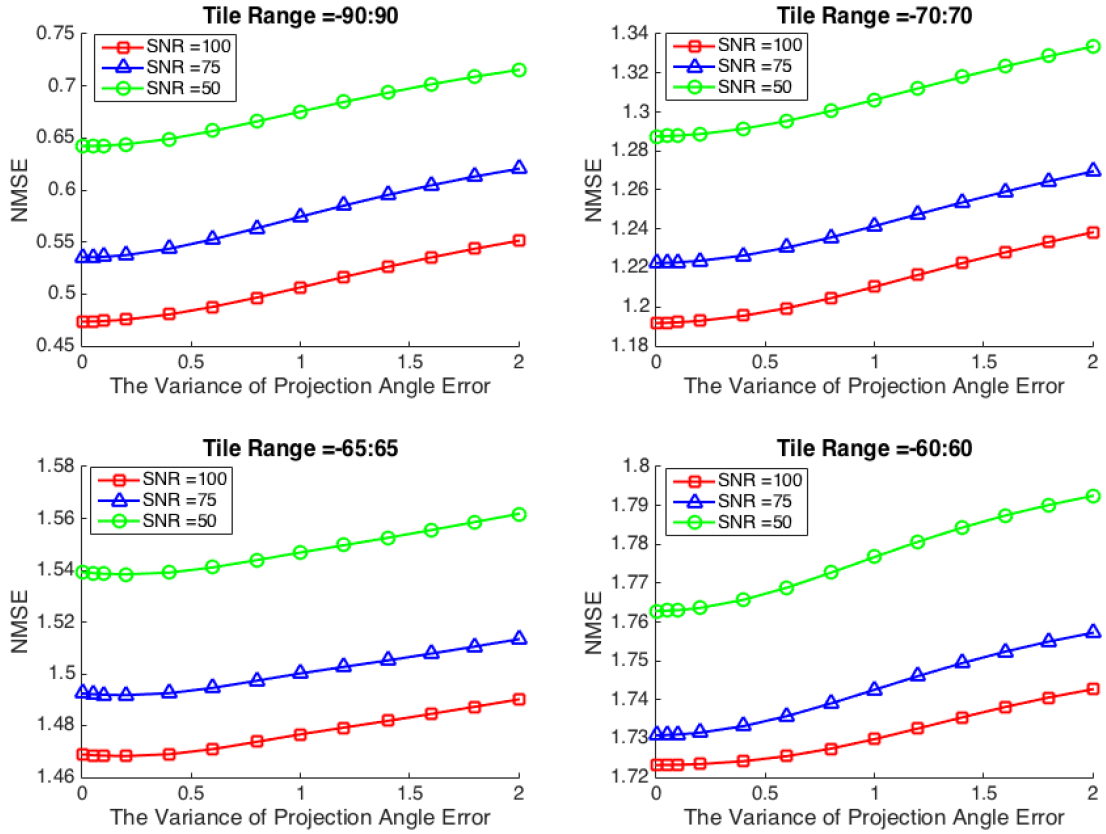**Figure 4.3** *The projection data with and without noise*

Figure 4.4 *The NMSE of FIRM with different parameter settings*

eter settings in section 4.1.3, the NMSE curve is shown in Figure 4.4.As we see from the figure, the tilt range is the main factor that effects the reconstruction performance. That is, as the tilt range decreasing, the NMSE is increasing regardless of SNR and projection angle error. Besides, another common sense is that, the more noise in the projection the more NMSE for reconstructed volume within same tilt range. However, Figure 4.4 shows an interesting discovery. Althogh the NMSE is increasing when the variance of projection angle error in the range of 0.5 to 2.0, the NMSE does not change obviously when the variance is below 0.3.

To observe the most realistic case where title range is $(-60°, 60°)$, we take a deep look at the last subplot figure in Figure 4.5. Since we already know the NMSE will keep increasing when VPE is large than 1.4, we only show the VPE in the range of (0.0, 1.4) to focus the effect of low VPE. Specifically, the NMSE is nearly unchange when VPE is below 0.4 and SNR equals to 100. However, the NMSE starts to increase when VPE equals to 0.2 if SNR equals to 75 or 100. Although the tilt

range is the primary factor that effects the NMSE, the reconstruction performance will further affected by VPE when VPE is large than 0.4. Moreover, even if the VPE is low, the NMSE also increases when the noise level is high.
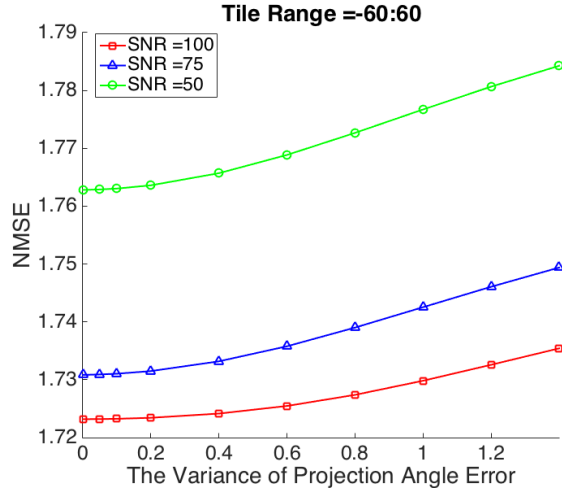

Figure 4.5 *The NMSE of FIRM in most realistic case, tilt range* $= (-60°, 60°)$

4.3 3D Alignment Experiments

In this work, we also use 3D Fourier Shell Correlation (FSC) to evaluate the reconstruction performance and alignment problem. FSC measures the normalized cross-correlation coefficient between two 3D volumes over corresponding spherical shells in Fourier space [46], i.e.,

$$FSC(j) = \frac{\sum_{\mathbf{i} \in Shell_j} \mathscr{F}(\mathbf{V}_b)(\mathbf{i}) \cdot \overline{\mathscr{F}(\mathbf{V})(\mathbf{i})}}{\sqrt{\sum_{\mathbf{i} \in Shell_j} |\mathscr{F}(\mathbf{V}_b)(\mathbf{i})|^2 \cdot \sum_{\mathbf{i} \in Shell_j} |\mathscr{F}(\mathbf{V})(\mathbf{i})|^2}}, \tag{4.5}$$

where $\mathscr{F}$ is the operation of Fourier transform, the spatial frequency j ranges from 1 to $N/2-1$ time the unit frequency $1/(N \cdot pixelsize)$, and $Shell_j := \mathbf{i} : 0.5 + (j-1) + \epsilon \leq \|\mathbf{i}\| \leq 0.5 + j + \epsilon$ where $\epsilon = 1e - 4$.

The FSC curves for the tilt ranges $\pm 90°$ and $\pm 60°$ are shown in Figure 4.7(a) and Figure 4.7(b) respectively. As a result we observe the spatial resolution is smaller with less VPE. The red line in each figure is the FSC threshold line. This line is used for equally compare the resolution of each reconstructed volume with different
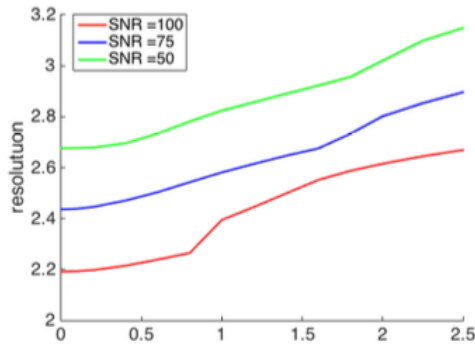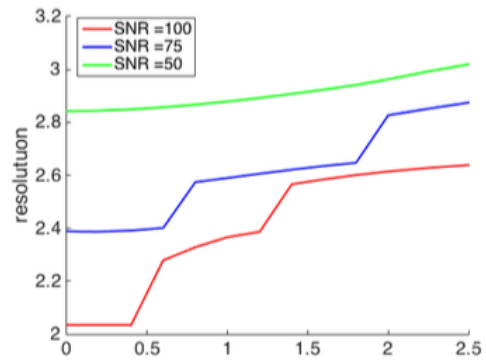
(a) The resolution curve under different SNR and VPE with tilt range from 90° to 90°
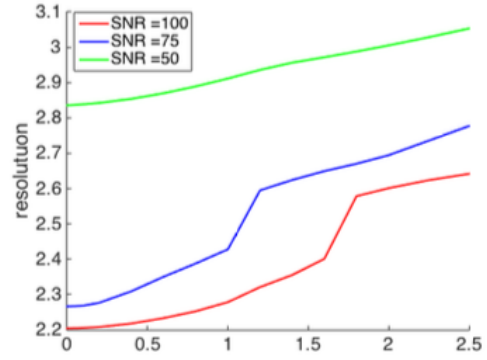
(b) The resolution curve under different SNR and VPE with tilt range from 70° to 70°
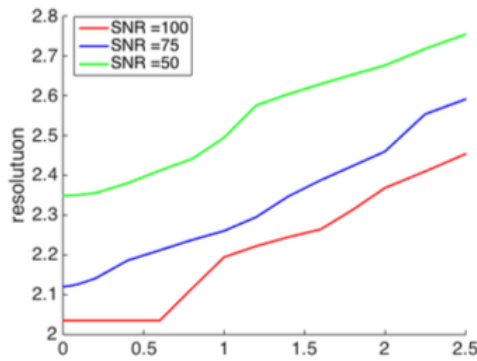
(c) The resolution curve under different SNR and VPE with tilt range from 65° to 65°

(d) The resolution curve under different SNR and VPE with tilt range from 60° to 60°

Figure 4.6 *The resolution curve with FSC threshold = 0.5*

parameters. As we see from Figure 4.7, the FSC threshold has to change in order to make a clear comparison for different tilt ranges.

In Figure 4.6, we show the resolution regarding to four groups of tilt ranges. First of all, the obvious thing is that the resolution is smaller as the SNR is higher. So that, the reconstructed volume is more unambiguous. Second, as the VPE increase, the resolution is higher as well. However, when the tilt range is small (±60° and ±65°), the resolution does not change very much with little VPE, this discovery is similar as we have seen in Figure 4.4.
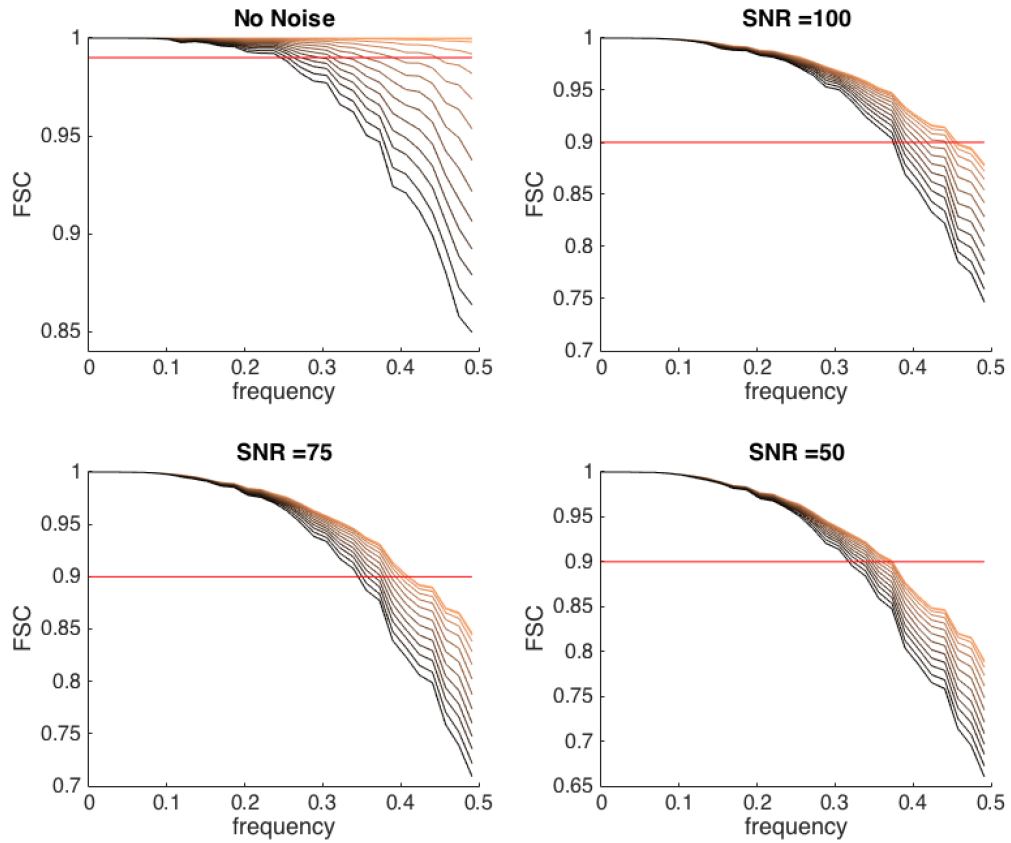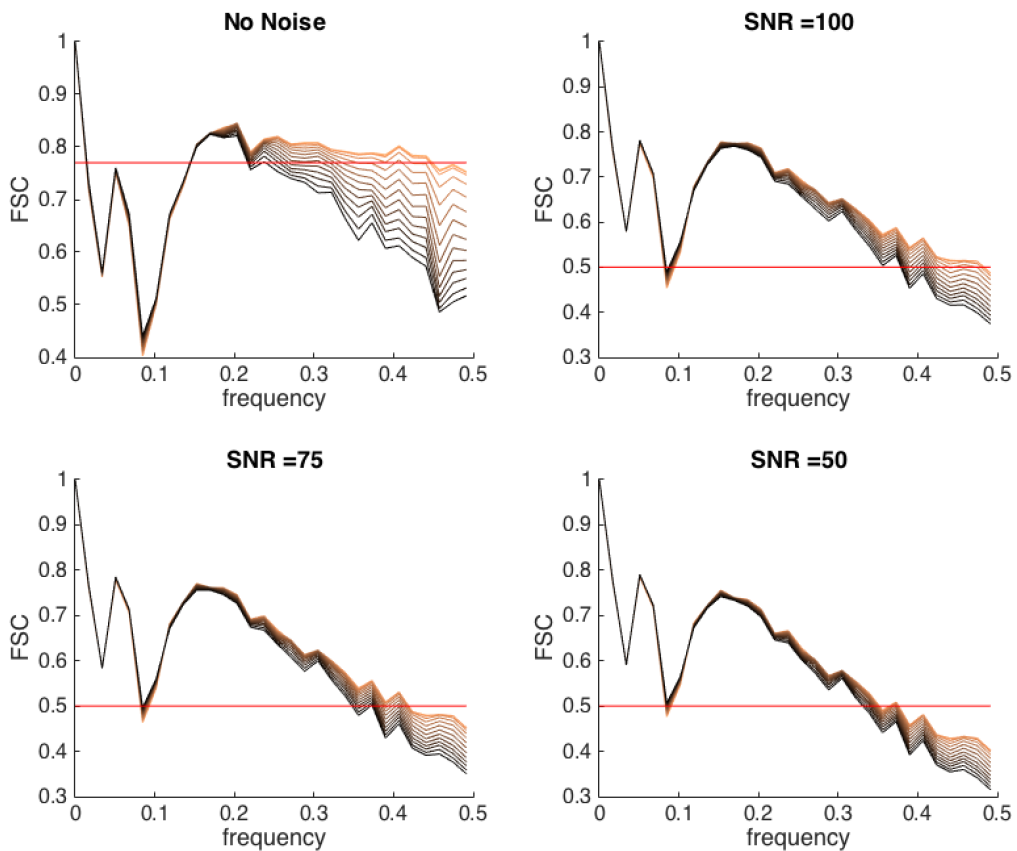
(a) The FSC curve under different SNR and VPE with tilt range from −90° to 90°

(b) The FSC curve under different SNR and VPE with tilt range from −60° to 60°

Figure 4.7 *The FSC curves with different parameters, FSC threshold lines are shown with red. In the each figure, the color of different line represent different variance of projection angle error (VPE), and the VPE increases as the color from yellow to dark. (In each curve, the resolution curve is calculated when the spatial frequency larger than 0.15)*

4.4   Experiments Summary

In previous sections, we give the numercal results with different parameter settings. In this section, we give the reconstructions in different cases to observe the impact of those three different factors, noise, missing wedge and projection angle error. To simplify the layout and make a clear observastion, only four slices of reconstruction are shown in each case.

At first, the impact of noise is given in Figure 4.8. The Gaussian noise is added in tilt series, so that the resulting reconstrcution contains noise points compared to the ideal case. Then, the impact of missing wedge and projection angle error is shown in Figure 4.9. In the missing wedge case, there are artifacts in the 17th slice. Moreover, the 33th and 41th are totally blurred, the objects in the phantom are hardly to observe compared to the same slices in Figure 4.8(a). The reason is that, there is less information about the phantom for reconstruction algorithm to fully reconstruct the ground truth. Whereas, the impact of miss alignment is less than missing wedge. However, there are still certain number of wave shape artifacts in the upper and lower side in each slice. Based on these figures, we find that the miss alignment has less effect than missing wedge when VPE = 2.5 and tilt range is $[-60°,60°]$.

Considering the reconstruction is much more unclear in missing wedge case in Figure 4.9(a), and FIRM cannot solve the miss wedge problem. Thus, we show the effect of miss alignment within full tilt range in Figure 4.10. By comparing Figure 4.10(a) and Figure 4.10(b), we find that increasing VPE from 0.2 to 2.5 has slight differences that human eye can recognize on the recontructions. Only in 33th slice, we find more noise in the circular object.
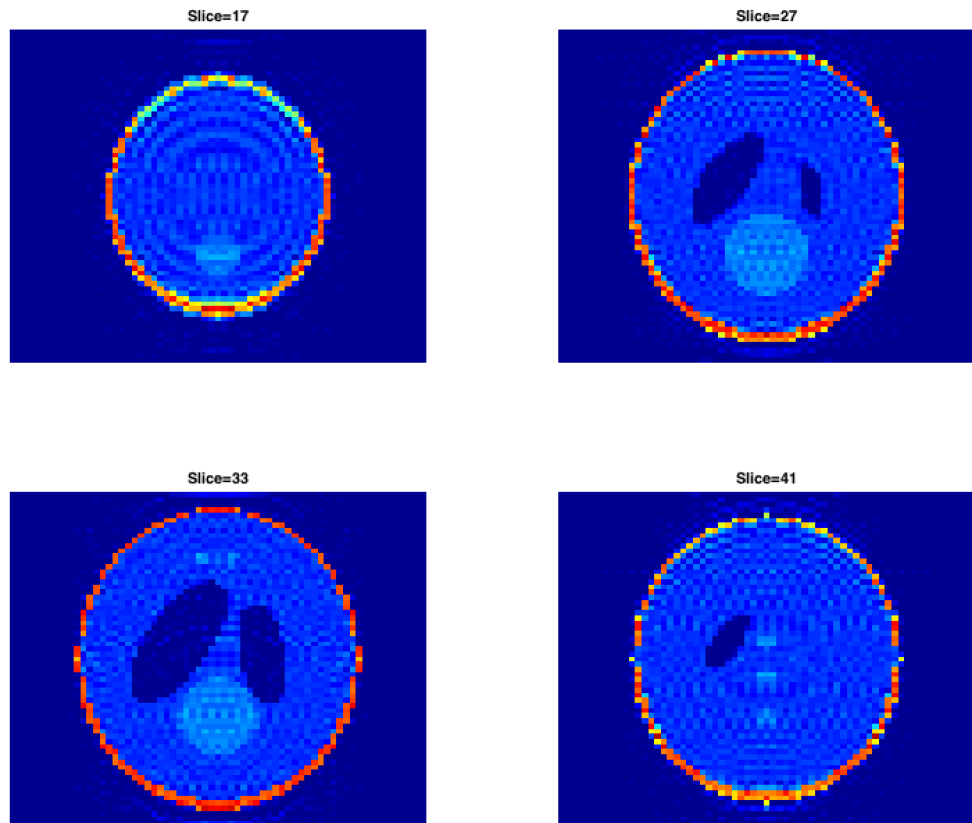
(a) The reconstruction in ideal case
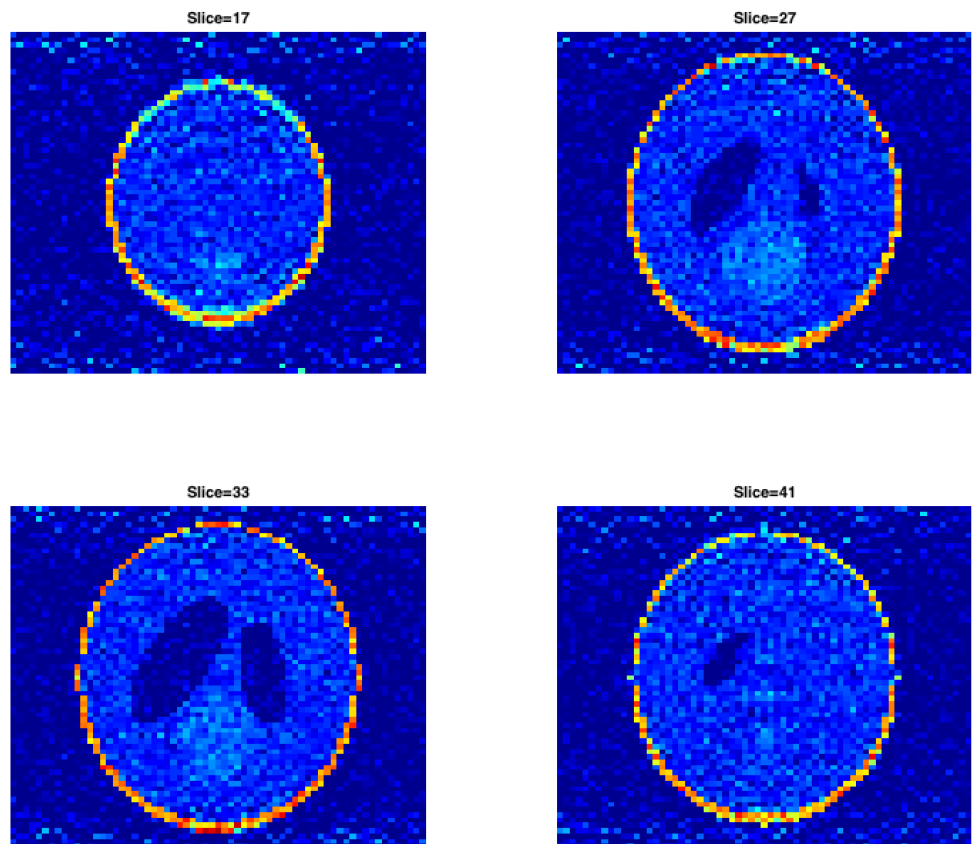
(b) The reconstruction with SNR = 50

Figure 4.8 *The comparison of reconstuctions between two cases: (a) Ideal case: full tilt ranges without noise and projection angle error; (b) Noise case: only noise are introduced in projection images, SNR = 50.*
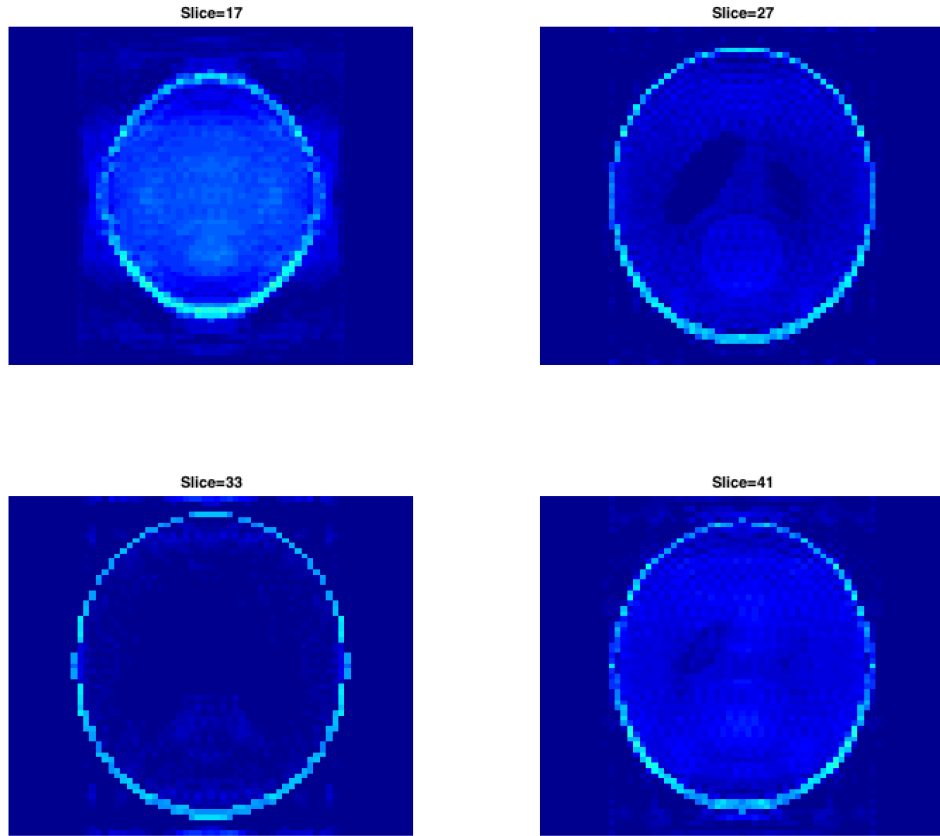
(a) The reconstruction with tilt range from $-60°$ to $60°$
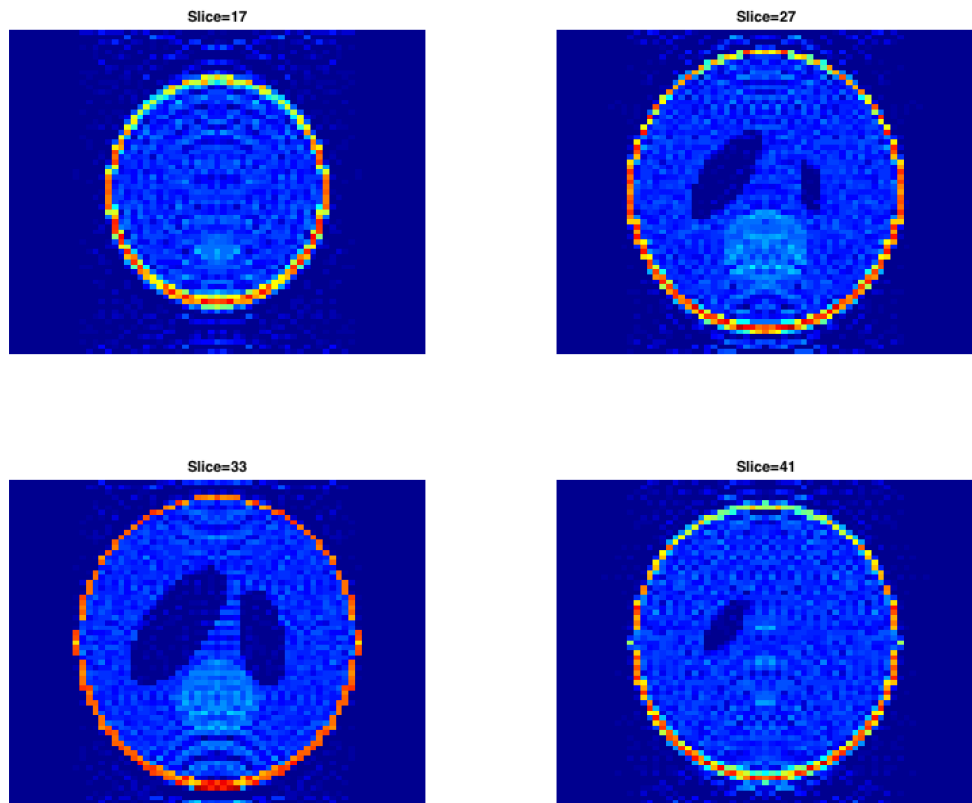
(b) The reconstruction with VPE = 2.5

Figure 4.9 *The comparison of reconstuctions between two cases: (a) Missing wedge case: only the tilt range is limited from $-60°$ to $60°$; (b) Projection angle error case: only variance of projetion angle error is set to be 2.5.*
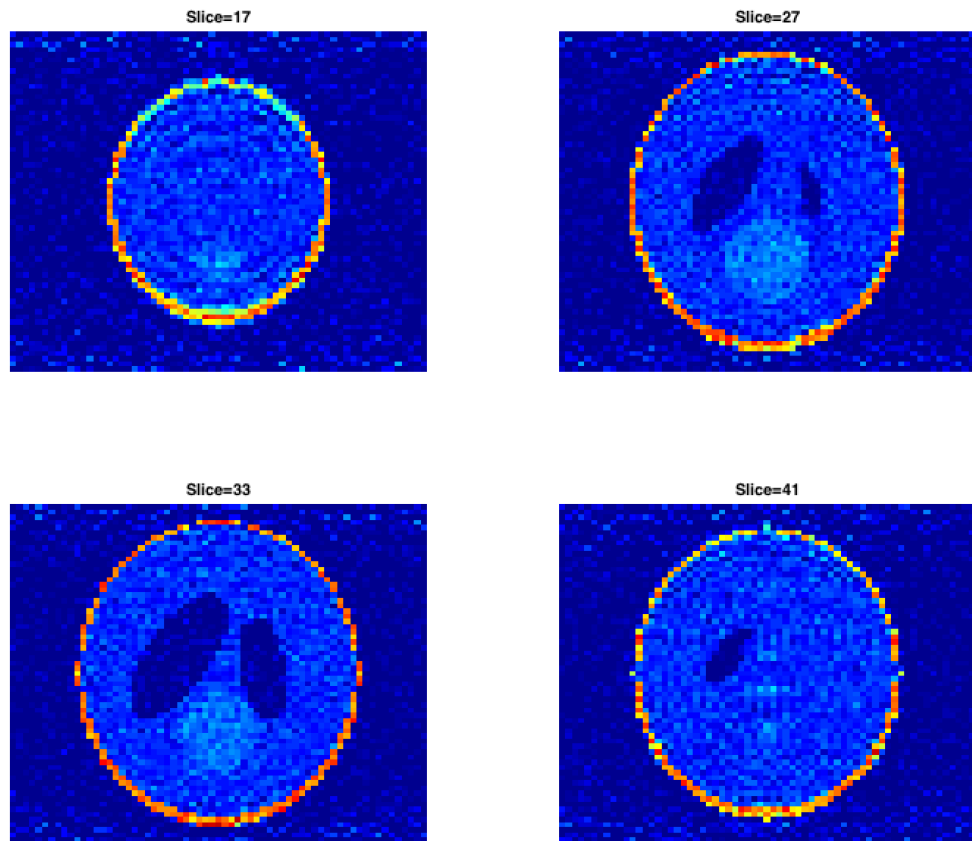
(a) The reconstruction with low VPE
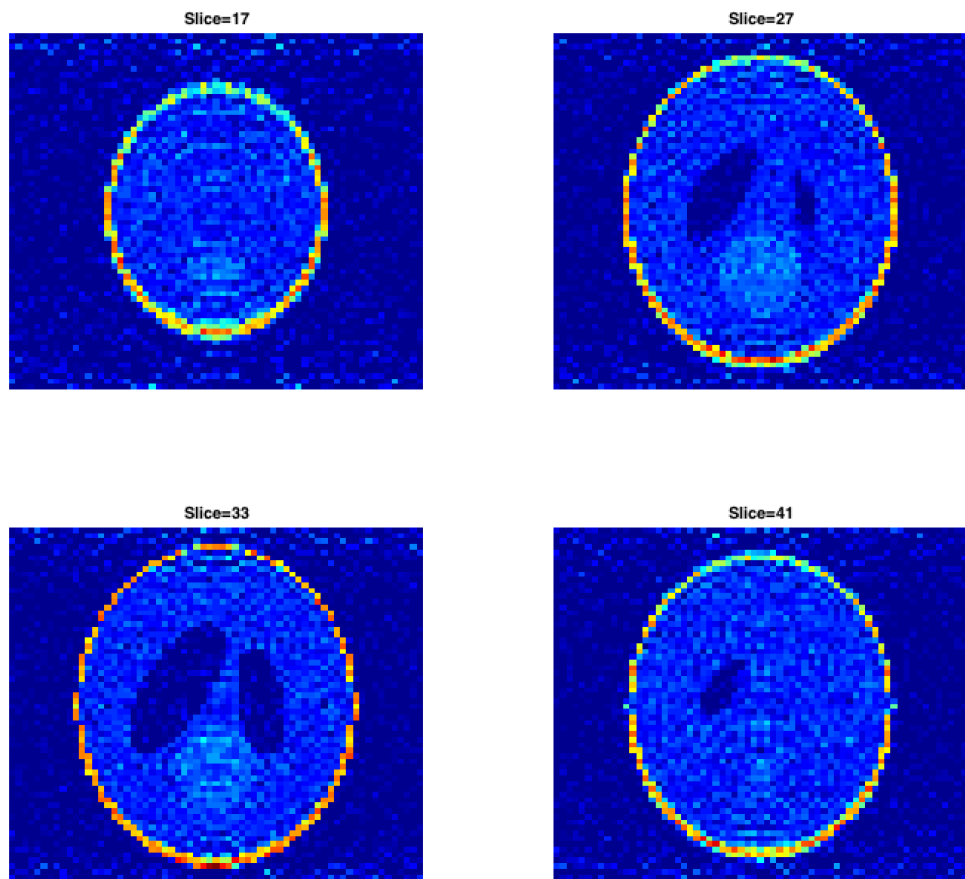
(b) The reconstruction with high VPE

Figure 4.10 *The comparison of reconstuctions between two different VPE settings: (a) Low VPE case: full tilt range, SNR = 100, VPE = 0.2; (b) High VPE case: full tilt range, SNR = 100, VPE = 2.5.*

5. CONCLUSION

The aim of this thesis is to characterize alignment problem in 3D eletron tomography. In order to complete this work, the whole experiment can be divided into three parts:

1. In data acquisition, we use min-max interpolated NUFFT to get simulated projection images;

2. In practical simulation, we introduce and analyze alignment problem in 3D electron tomography;

3. In reconstrcution experiment, Fourier-based iterative reconstruction method is the mainly used way to get 3D volume from noisy and miss aligned data.

We have seen how to get projection images in 3D electron tomography. Unlike traditional digitalized Radon transform in 3D casde, NUFFT with min-max is a faster and more accurate way to simulate projection data in frequency domain. However, there are still challenges in finding more optimal interpolator, so that the projection data may not be exactly the same as projection images in practice.

During data acquisition, the volume is projected with ill-posed projection angles in limited tilt range. However, the ratotation matrix used in reconstruction is calculated with predefined projection angles. In such way, the reconstruction method needs to align data during reconstruction in a refinement way.

Fourier-based iterative method (FIRM) reconstructs 3D volume in frequency domain by using NUFFT. By using conjugate gradient (CG), FIRM is converged fast in 100 iterations. However, as the tilt range decreases the missing wedge effect enlarges, more iterations are needed to get optimal reconstructions. When the projection angle error does not vary too much (within 0.2 variance change), the reconstructed 3D volume has little changes which was measured both with normalized mean square error (NMSE) and Fouirer shell correlation (FSC).

In current situation, we found missing wedge is the main factor that affects the reconstruction performance. Without powerful reconstruction methods to compensate the missing gaps, the reconstruction volume is sharply blurred. Whereas, miss alignment has less effect compared to missing wedge. Although increasing VPE causes error in reconstructions, less differences are found by human eyes.

In the further work, more precise method that collects projection data is needed in simulation part. In severe situations when there are certain gaps in Fourier space (the missing wedge effect), regularization can alleviate the ill-conditioning of the problem. If prior knowledge about the 3D volume is avaible during reconstruction, this method may works better.

BIBLIOGRAPHY

[1] J. Frank, "Electron tomography: Methods for three-dimensional visualization of structures in the cell," Springer, 2006.

[2] P. Gilbert, "Iterative methods for the three-dimensional reconstruction of an object from projections," *Journal of theoretical biology*, vol. 36, no. 1, pp. 105–117, 1972.

[3] M. Unser, C. S. Sorzano, P. Thevenaz, S. Jonić, C. El-Bez, S. De Carlo, J. Conway, and B. Trus, "Spectral signal-to-noise ratio and resolution assessment of 3d reconstructions," *Journal of structural biology*, vol. 149, no. 3, pp. 243–255, 2005.

[4] S. Bals, S. Van Aert, and G. Van Tendeloo, "High resolution electron tomography," *Current Opinion in Solid State and Materials Science*, vol. 17, no. 3, pp. 107–114, 2013.

[5] L. F. Drummy and C. Kübel, "Polymer microscopy: Current challenges," *Polymer Reviews*, vol. 50, no. 3, pp. 231–234, 2010.

[6] R. Leary, P. A. Midgley, and J. M. Thomas, "Recent advances in the application of electron tomography to materials chemistry," *Accounts of Chemical Research*, vol. 45, no. 10, pp. 1782–1791, 2012.

[7] M. Radermacher, T. Wagenknecht, A. Verschoor, and J. Frank, "A new 3-d reconstruction scheme applied to the 50s ribosomal subunit of e. coli," *Journal of Microscopy*, vol. 141, no. 1, pp. RP1–RP2, 1986.

[8] S. Horbelt, M. Liebling, and M. A. Unser, "Filter design for filtered back-projection guided by the interpolation model," in *Medical Imaging 2002*, pp. 806–813, International Society for Optics and Photonics, 2002.

[9] L. Paavolainen, E. Acar, U. Tuna, S. Peltonen, T. Moriya, P. Soonsawad, V. Marjomäki, R. H. Cheng, and U. Ruotsalainen, "Compensation of missing wedge effects with sequential statistical reconstruction in electron tomography," 2014.

[10] K. J. Batenburg and J. Sijbers, "Dart: a practical reconstruction algorithm for discrete tomography," *Image Processing, IEEE Transactions on*, vol. 20, no. 9, pp. 2542–2553, 2011.

[11] K. Batenburg, S. Bals, J. Sijbers, C. Kübel, P. Midgley, J. Hernandez, U. Kaiser, E. Encina, E. Coronado, and G. Van Tendeloo, "3d imaging of nanomaterials by discrete tomography," *Ultramicroscopy*, vol. 109, no. 6, pp. 730–740, 2009.

[12] D. Chen, B. Goris, F. Bleichrodt, H. H. Mezerji, S. Bals, K. J. Batenburg, G. de With, and H. Friedrich, "The properties of sirt, tvm, and dart for 3d imaging of tubular domains in nanocomposite thin-films and sections," *Ultramicroscopy*, vol. 147, pp. 137–148, 2014.

[13] B. Goris, T. Roelandts, K. Batenburg, H. H. Mezerji, and S. Bals, "Advanced reconstruction algorithms for electron tomography: from comparison to combination," *Ultramicroscopy*, vol. 127, pp. 40–47, 2013.

[14] E. J. Candè and M. B. Wakin, "An introduction to compressive sampling," *Signal Processing Magazine, IEEE*, vol. 25, no. 2, pp. 21–30, 2008.

[15] D. L. Donoho, "Compressed sensing," *Information Theory, IEEE Transactions on*, vol. 52, no. 4, pp. 1289–1306, 2006.

[16] L. Wang, Y. Shkolnisky, and A. Singer, "A fourier-based approach for iterative 3d reconstruction from cryo-em images," *arXiv preprint arXiv:1307.5824*, 2013.

[17] X. Li, D. Zhang, and B. Liu, "A generic geometric calibration method for tomographic imaging systems with flat-panel detectors a detailed implementation guide," *Medical physics*, vol. 37, no. 7, pp. 3844–3854, 2010.

[18] M.C.Lawrence, "Least-squares method of alignment using markers," in *ElectronTomography: Three Dimensional Imaging with the Transmission Electron Microscope* (J. Frank, ed.), pp. 197–204, New York: Plenum, 1992.

[19] S. S. Brandt and V. Kolehmainen, "Structure-from-motion without correspondence from tomographic projections by bayesian inversion theory," *Medical Imaging, IEEE Transactions on*, vol. 26, no. 2, pp. 238–248, 2007.

[20] R. Hartley and A. Zisserman, *Multiple view geometry in computer vision*. Cambridge university press, 2003.

[21] P. Penczek, M. Radermacher, and J. Frank, "Three-dimensional reconstruction of single particles embedded in ice," *Ultramicroscopy*, vol. 40, no. 1, pp. 33–53, 1992.

[22] C. Yang, E. G. Ng, and P. A. Penczek, "Unified 3-d structure and projection orientation refinement using quasi-newton algorithm," *Journal of structural biology*, vol. 149, no. 1, pp. 53–64, 2005.

[23] L. Houben and M. B. Sadan, "Refinement procedure for the image alignment in high-resolution electron tomography," *Ultramicroscopy*, vol. 111, no. 9, pp. 1512–1520, 2011.

[24] J. Navaza, "On the three-dimensional reconstruction of icosahedral particles," *Journal of structural biology*, vol. 144, no. 1, pp. 13–23, 2003.

[25] Z. Yin, Y. Zheng, P. C. Doerschuk, P. Natarajan, and J. E. Johnson, "A statistical approach to computer processing of cryo-electron microscope images: virion classification and 3-d reconstruction," *Journal of structural biology*, vol. 144, no. 1, pp. 24–50, 2003.

[26] Fessler, "Fundamentals of ct reconstruction in 2d and 3d," in *Comprehensive Biomedical Physics, Vol. 2: X-Ray and Ultrasound Imaging* (A. Brahme, ed.), pp. 263–95, Elsevier, Netherlands, 2014.

[27] A. Kak and M. Slaney, "Principles of computerized tomography (piscataway, nj: Ieee)," 1987.

[28] T. Epicier, *3D nanoimaging of semiconductor devices and materials by electron tomography.* PhD thesis, CEA, LETI, 2013.

[29] J. Fessler, "Statistical iterative reconstruction for x-ray computed tomography," in *Biomedical Mathematics: Promising Directions in Imaging, Therapy Planning and Inverse Problems* (Y. Censor, M. Jiang, and G. Wang, eds.), pp. 113–40, Medical Physics Publishing,Madison, 2010.

[30] R. Ng, "Fourier slice photography," in *ACM Transactions on Graphics (TOG)*, vol. 24, pp. 735–744, ACM, 2005.

[31] S.-R. Zhao and H. Halling, "Reconstruction of cone beam projections with free source path by a generalized fourier method," in *1995 International Meeting on Fully Thee-Dimensional Image Reconstruction in Radiology and Nuclear Medicine*, p. 323, 1995.

[32] D. Zosso, M. Bach Cuadra, and J.-P. Thiran, "Direct fourier tomographic reconstruction image-to-image filter," tech. rep., 2007.

[33] D. Wolf, A. Lubk, and H. Lichte, "Weighted simultaneous iterative reconstruction technique for single-axis tomography," *Ultramicroscopy*, vol. 136, pp. 15–25, 2014.

[34] Frank, *Three-dimensional electron microscopy of macromolecular assemblies: visualization of biological molecules in their native state*. Oxford University Press, 2006.

[35] J. Fessler, B. P. Sutton, *et al.*, "Nonuniform fast fourier transforms using min-max interpolation," *Signal Processing, IEEE Transactions on*, vol. 51, no. 2, pp. 560–574, 2003.

[36] F. Natterer, *The mathematics of computerized tomography*, vol. 32. Siam, 1986.

[37] H. Stark, J. W. Woods, I. Paul, and R. Hingorani, "Direct fourier reconstruction in computer tomography," *Acoustics, Speech and Signal Processing, IEEE Transactions on*, vol. 29, no. 2, pp. 237–245, 1981.

[38] T. Hastie, R. Tibshirani, J. Friedman, and J. Franklin, "The elements of statistical learning: data mining, inference and prediction," *The Mathematical Intelligencer*, vol. 27, no. 2, pp. 83–85, 2005.

[39] Y. Saad, *Iterative methods for sparse linear systems*. Siam, 2003.

[40] Z. Yang, J. Fang, J. Chittuluru, F. J. Asturias, and P. A. Penczek, "Iterative stable alignment and clustering of 2d transmission electron microscope images," *Structure*, vol. 20, no. 2, pp. 237–247, 2012.

[41] R. Beckmann, D. Bubeck, R. Grassucci, P. Penczek, A. Verschoor, G. Blobel, and J. Frank, "Alignment of conduits for the nascent polypeptide chain in the ribosome-sec61 complex," *Science*, vol. 278, no. 5346, pp. 2123–2126, 1997.

[42] B. Vainshtein and P. Penczek, "Three-dimensional reconstruction," *International Tables for Crystallography*, vol. 3, pp. 366–375, 2006.

[43] P. A. Penczek, "Chapter one-fundamentals of three-dimensional reconstruction from projections," *Methods in enzymology*, vol. 482, pp. 1–33, 2010.

[44] J. B. Kuipers, *Quaternions and rotation sequences*, vol. 66. Princeton university press Princeton, 1999.

[45] B. Palais, R. Palais, and S. Rodi, "A disorienting look at euler's theorem on the axis of a rotation," *The American Mathematical Monthly*, pp. 892–909, 2009.

[46] M. van Heel and M. Schatz, "Fourier shell correlation threshold criteria," *Journal of structural biology*, vol. 151, no. 3, pp. 250–262, 2005.